An Investigation of Surface Heat Fluxes

during El Niño – Southern Oscillation (ENSO) Evolution

in Reanalyses

by

Nicole D. Colasacco-Thumm

A thesis submitted in partial fulfillment of

the requirements for the degree of

Master of Science

(Atmospheric and Oceanic Sciences)

at the

UNIVERSITY OF WISCONSIN-MADISON

2015

Approved: _____

Daniel J. Vimont

Associate Professor, Department of Atmospheric and Oceanic Sciences

Date: _____

Abstract

The role of surface heat flux anomalies in ENSO (El Niño-Southern Oscillation) is primarily believed to be one of dampening during the decay of an ENSO event with no noteworthy contributions to the development of an ENSO event. Recent developments of more advanced high-resolution reanalyses (gridded data products combining models and observations) provide an opportunity to investigate ENSO (El Niño-Southern Oscillation) related surface heat flux variations in greater detail. The purpose of this thesis is two-fold: to diagnose how surface heat flux variations affect the evolution of ENSO using reanalyses, and to qualitatively evaluate and compare reanalyses in the tropical and subtropical Pacific using ENSO.

This thesis shows the spatial structure of different components of the surface heat flux has a much richer structure and evolving relationship with SST during the development of an ENSO event than previously believed. While the evolution of some variables is much more clearly depicted in the more advanced reanalysis (e.g. precipitation), components of the heat flux budget (in particular shortwave radiation) still remain a source of significant variability among reanalyses.

Acknowledgments

I'd like to thank my advisor, Dan Vimont. For not only providing me with invaluable scientific support, advice, and discussions, but also giving me such a supportive working environment. I am truly grateful to have worked with an advisor that is both an exceptional scientist and a thoughtful caring person.

Thank you my research group: Anne-Sophie Daloz, Cristian Martinez, Erin Thomas, Ross Dixon, and Megan Kirchmeier-Young. Their support and willingness to assist even when I was working remotely is truly appreciated. I think it is rare that one finds such a supportive and collaborative group and it has been a privilege to be a part of it.

I'd also like to thank my readers: Galen Mckinley and Ankur Desai for taking the time to give constructive criticism and feedback on this thesis. It is greatly appreciated. Thank you to all the staff and faculty here in Madison who have helped me throughout my time at UW Madison.

I would like to thank my husband, Stephen, for his support and understanding throughout. I know at times this wasn't easy and I thank you for being so even keeled. You are my rock. Thank you to my mother for always being there when I need you whether it be proofreading or listening to my frustrations. I'd like to thank my daughter, Domenica, for recapturing my sense of wonder and allowing me to look at life anew through your eyes. And last, above all I'd like to thank God.

Table of Contents

List of Figures

1.   Introduction

The El Niño-Southern Oscillation (ENSO) phenomenon is the largest source of year-to-year climate variability on Earth. Positive ENSO events (El Niño events) are characterized by: warming sea surface temperatures (SST), decreased sea level pressure, and a deepening thermocline in the eastern Pacific; increased sea level pressure in the western Pacific; a relaxation of the tradewinds; and a shift of convection from the west to central Pacific; (Rasmusson and Carpenter 1982; Deser and Wallace 1990; Harrison and Larkin 1996, 1998; Wallace et al. 1998; McPhaden 2004). Negative ENSO events (La Niña events) involve the opposite features, though ENSO is not purely a linear phenomenon (Larkin and Harrison 2002; Okumura and Deser 2010).

El Niño-Southern Oscillation has been well established as having a defined seasonal phase locking. It develops during the boreal summer and fall, peaks during the boreal winter and begins decaying in the boreal spring. Numerous studies have described the seasonal cycle (e.g. Rasmusson and Carpenter 1982; Larkin and Harrison 2002). However, there are fewer studies that diagnose the seasonal evolution of ENSO-related surface heat flux variations. These variations play an important role in the development and decay of various features associated with developing ENSO events. In general, SST anomalies during ENSO events are thought to be primarily dynamically driven, with surface heat flux anomalies acting to damp anomalies (Barnett et al. 1991; Wang and McPhaden 2000; Zhang et al. 2007). With the recent development of more advanced high-resolution reanalyses (gridded data

products combining models and observations), there is an opportunity to investigate ENSO related surface heat flux variations in greater detail. As shown in this study, the spatial structure of different components of the surface heat flux has a much richer structure and evolving relationship with SST during the development of an ENSO event. While the evolution of some variables is much more clearly depicted in the more advanced reanalysis (e.g. precipitation), components of the heat flux budget (in particular shortwave radiation) still remain a source of significant uncertainty among reanalyses.

The study has two major objectives. The first is to investigate ENSO evolution in the reanalyses with emphasis on the surface heat flux. The second is to use ENSO to qualitatively compare and evaluate reanalyses in the tropical and subtropical Pacific.

1.1.   ENSO Background

ENSO is the largest source of climate variability in the Pacific. One of the defining features of an El Niño (La Niña) is the increase (decrease) in sea surface temperature (SST) in the eastern and central Pacific Ocean. A commonly used index for defining ENSO events is SST anomalies in the Niño3.4 region (Barnston et al. 1997). The Niño3.4 is the deviation from the mean climatology of the SST in an area bounded by 5°N -5°S, 170°-120°W (**Figure 1**). Strong El Niño events tend to have peak SST anomalies of 2° C or greater for several months; moderate El Niño anomalies range from 1° C to 2° C. La Niña events are slightly weaker.

ENSO events follow a distinct seasonal pattern. **Figure 2** shows the Niño3.4 SST deviations for seven El Niño events and eight La Niña events. Although there is individual variation in each event, the overall pattern shows a distinct seasonal evolution during ENSO events with Niño3.4 SST deviations intensifying from May to October, reaching a peak from November to January, and decaying from February through June. In this study, ENSO events are defined as a standard deviation of one or more from the 1979-2009 Niño3.4 between the seasons of August-September-October to February-March-April. A composite of the seven El Niño events and the eight La Niña events where the events are defined as a standard deviation of one or more from the average between ASO and FMA is also shown in **Figure 2**. **Figure 3** gives the variance for each three-month season. November-December-January (NDJ) is defined as the peak has the most variance and is the peak season.

The seasonal evolution of ENSO has been well documented (e.g. Rasmusson and Carpenter 1982; Deser and Wallace 1990; Harrison and Larkin 1998; Harrison and Vecchi 1999). In a neutral year, there is a cold tongue in the eastern Pacific, high sea level pressure in the eastern Pacific/ low sea level pressure in the western Pacific and strong tradewinds north and south of the equator. During the development of El Niño, major developments include: warming SST along the equator in the eastern and central Pacific; increased thermocline depth in the eastern Pacific; intensification of the Intertropical Convergence Zone (ITCZ), large westerly wind anomaly west of the dateline; reversal of the sea level pressure gradient in the tropical Pacific (Southern Oscillation); and a reduction in or reversal

of the easterly trade winds. This state generates a positive feedback (Bjerknes 1969) in which warmer SST in the eastern Pacific leads to decreased surface pressures in the eastern Pacific and decreased easterly winds. These decreased winds reduce upwelling creating warmer SST reinforcing the cycle. As the ENSO event peaks (NDJ), the warmer SSTs broaden meridionally, the reversal of sea level pressure intensifies, easterly trade winds near the dateline continue to decrease and even reverse, maritime continent/western Pacific precipitation shifts eastward, and the ITCZ and South Pacific Convergence Zone intensify and shift equatorward. Important features in the decay of an El Niño include: shifting of westerly wind anomalies south of equator; continued equatorward shift of Convergence Zones (CZ); shoaling of the eastern Pacific thermocline and sharply decreased SST anomalies in the eastern Pacific; reduced Southern Oscillation. La Niña events follow an opposite evolution though nonlinearities do exist between positive and negative events(Larkin and Harrison 2002; Okumura and Deser 2010).
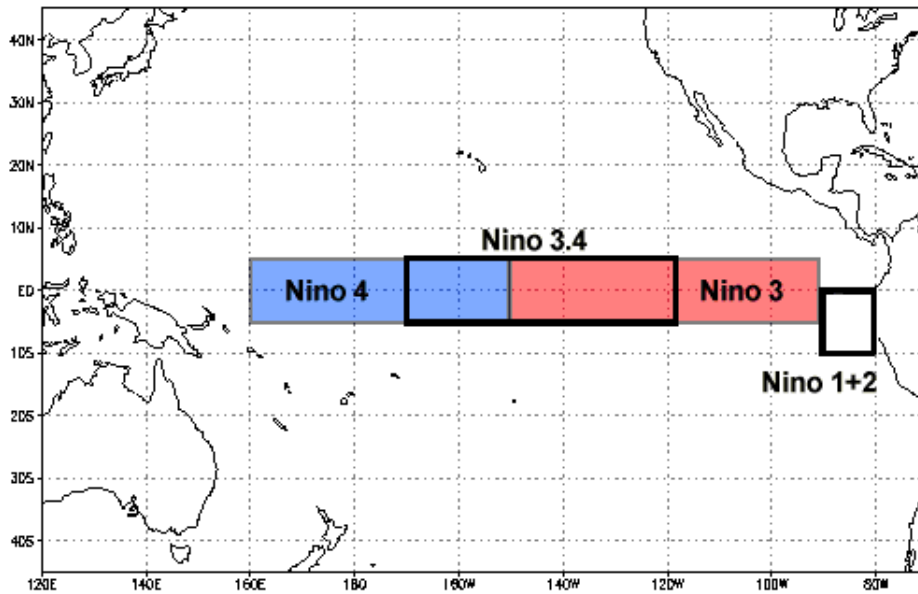
Figure 1: Location of Nino3.4
Source: "Equatorial Pacific Sea Surface Temperatures | National Centers for Environmental Information (NCEI)," n.d.
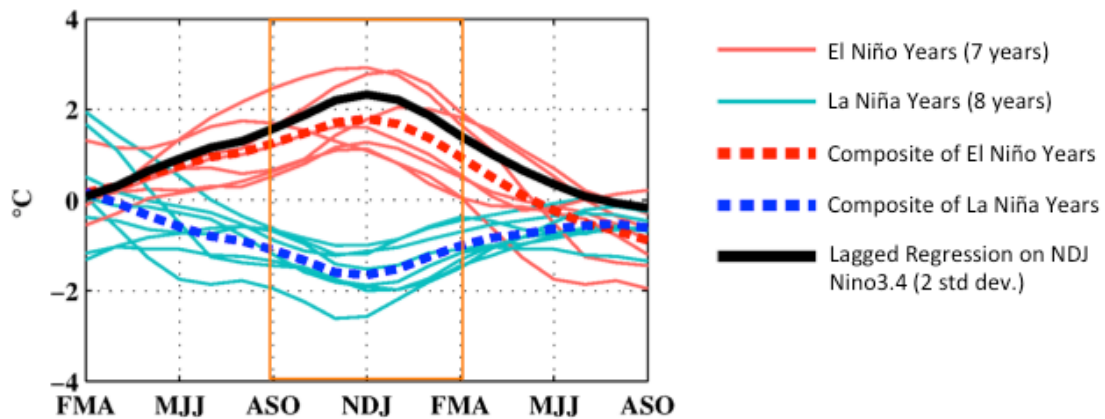
Figure 2: Seasonal Evolution of ENSO
El Nino years are: 82/83, 87/88, 91/92, 94/95, 97/98, 02/03, 06/07
La Nina Years are: 83/84, 84/85, 88/89, 95/96, 98/99, 99/00, 00/01, 07/08.
All data is the mean of the five models.
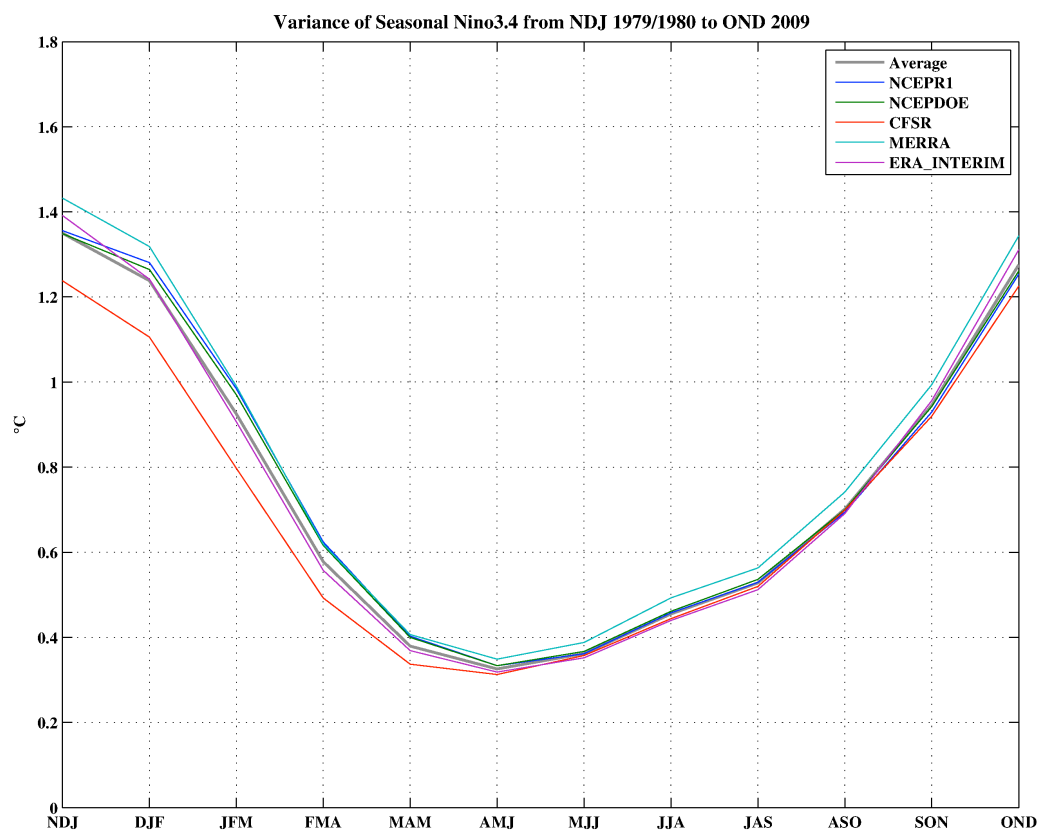
Figure 3: Seasonal Variance of Nino3.4

1.2. Reanalysis Background

Reanalyses are gridded data products that are the result of model assimilation of observations. Reanalyses use an atmospheric general circulation model to assimilate observations from multiple data sources. In contrast with most datasets, they have systematic spatial and temporal coverage. Reanalyses have become "the most widely used observational datasets in the atmospheric sciences" (Dee et al. 2011b). The first reanalysis, NCEP-NCAR R1 ((Kalnay et al. 1996), has been credited with being the most cited paper in all of climate science (Thorne and Vose 2010).

As with any dataset, reanalyses have some disadvantages. In data sparse regions reanalyses revert to the model physics. Furthermore, certain fields are heavily dependent on model parameterizations; for example, precipitation is not usually assimilated or carried as an element of the model state vector, and thus is heavily dependent on model parameterization. Biases can occur in the observation data, assimilation methods and model physics. Additionally, there is a struggle between creating the best possible dataset at each time step and creating a long-term homogeneous dataset. The introduction of new sets of observational data (e.g. new satellite radiances) can create jumps in the data record. All of these factors must be considered when evaluating the use of reanalyses in climate studies. (Thorne and Vose 2010; Dee et al. 2011b; Trenberth et al. 2011a; Bosilovich et al. 2012)

For this study, five different atmospheric reanalyses are used: NCEP-NCAR R1, NCEP-DOE, CFSR, MERRA and ERA-Interim. The time period for this study is 31

years (1979-2009). A common classification of reanalyses is the 'n-th generation reanalysis'. While distinctions among groups of reanalyses can be somewhat fuzzy, this is a method of categorizing the reanalyses into groups of major model developments. In this study, the NCEP-NCAR R1 and the NCEP-DOE are considered 1st generation reanalyses; the CFSR, MERRA, and ERA-Interim all are 3rd generation reanalyses that have significant updates in assimilating satellite radiances, advanced data assimilation approaches (4DVAR and incremental analysis), higher resolution, and in one model, the CFSR, coupling between the ocean and atmosphere (Trenberth et al. 2011b).

The following is a brief summary of the reanalysis products with an emphasis on the differences affecting the tropical and subtropical Pacific.

The NCEP-NCAR R1 (henceforth NCEPR1) is the first widely available reanalysis. The horizontal resolution is T62 (~208km) with a 28 layer vertical resolution. The NCEPR1 uses a three-dimensional variational data assimilation (3DVAR) assimilation scheme and a model (developed in 1995), which is kept frozen for the entire time period. A detailed description NCEPR1 including observations used can be found in Kalnay et al. (1996).

The NCEP-DOE R2 (henceforth NCEPDOE) is an update to the NCEPR1. The resolution is the same as the R1. It also uses a 3DVAR assimilation with model updates (developed in 2001) and is frozen for the time period. Major model updates relevant to heat flux and precipitation over the region of interest include an improved shortwave scheme, a more realistic ocean albedo (from .15 to .06-.07) and

improved cloud development (including convective parameterization). A more comprehensive description of these updates and information on the model can be found in Kanamitsu et al. (2002).

The CFSR is a 3rd generation NCEP reanalysis. It has a horizontal resolution of T382 and a 64 layer vertical resolution. It uses a more advanced 3DVAR assimilation scheme with Gridpoint Statistical Interpolation (GSI), which includes satellite radiances over the whole period, a coupled ocean-atmosphere, an interactive sea ice model, and the inclusion of observed CO_2 concentrations over the 1979-2009 time period. Saha et al. (2010) provides a complete description of the CFSR.

The MERRA is a 3rd generation NASA reanalysis. It has a horizontal resolution of ½° latitude × ⅔° longitude and a 72 layer vertical resolution. It uses the GEOS-5 atmospheric circulation model (Lin 2004).The data assimilation scheme is GSI 3DVAR with Integrated Analysis Updates (IAU) (Bloom et al. 1996) which incorporates analysis increments in the model thereby reducing forecast initialization due to observations. Rienecker et al. (2011) provides a complete description of the MERRA including information on the extensive satellite radiance products assimilated.

The ERA-Interim is the ECMWF's 3rd generation reanalysis update to the 2nd generation ERA 40. It has a horizontal resolution of T255 with a 60 layer vertical resolution. It uses the Integrated Forecast System (IFS) version Cy31r2. Significant updates include a 4DVAR data assimilation scheme, variational bias correction that automatically detects new satellite data streams and develops bias input without

manual interference (Dee and Uppala 2009), and an updated humidity scheme.
Additional information on this, details of the model physics updates and the satellite
radiances included can be found in Dee et al. (2011a).

1.3. Thesis Outline

The purpose of this thesis is twofold: 1) to diagnose how surface heat flux
variations affect the evolution of ENSO throughout it's cycle using reanalyses; and 2)
to qualitatively evaluate and compare reanalyses in the tropical and subtropical
Pacific using ENSO. The thesis is organized as follows. **Section 2** describes the data
and methods (primarily lagged linear regressions) used to study ENSO and the
reanalyses. **Section 3** shows the results of the lagged linear regression analyses and
diagnoses some of the differences in heat flux components. **Section 4** synthesizes
the major findings and provides suggestions for areas of future work.

2. Data & Methods

2.1. Data

In this study, the primary analysis area is the tropical Pacific from 30°N to
30°S, 100°E to 75°W. The variables examined are monthly precipitation, winds
(10m), skin temperature, air temperature (2m), sea-level pressure, specific
humidity (2m), and surface heat flux components (net shortwave, net longwave,
sensible heat flux and latent heat flux). All monthly data are obtained directly from
the respective reanalysis center with the exception of the ERA-Interim. For the ERA-
Interim, precipitation and surface heat components are based on twelve hour

accumulated indices; all other variables are monthly averages of six-hour data. All monthly anomalies are calculated by subtracting the monthly climatology for the thirty-one year period (1979-2009). The reanalysis model resolutions obtained for this study are as follows (latitude x longitude format): 1.905° x 1.875° for the NCEP-NCAR R1 and NCEP-DOE R2, 1.5° x 1.5° for the ERA-Interim, .5° x. 0.667° for the MERRA, and .5° x .5° for the CFSR.

This study examines the reanalyses' response to surface heat flux, surface heat flux components, and precipitation. These quantities are important in understanding the ocean-atmosphere feedbacks during ENSO evolution (Webster and Lukas 1992). In reanalyses surface fluxes and precipitation are derived fields and as such are dependent on the reanalyses parameterizations and physics biases in addition to uncertainties in the incorporated observations (Roberts et al. 2012). Because of these they are much more variable than fields constrained by observations (such as temperature). The surface heat flux is defined as

$$Q_{surface} = SW_{net} + LW_{net} + SH + LH$$

1)

where $Q_{surface}$ is the total surface heat flux, SW_{net} is the net Shortwave Radiation (Outgoing-Incoming), LW_{net} is the net Longwave Radiation (Outgoing – Incoming), SH is the Sensible Heat flux from the ocean to the atmosphere and LH is the Latent Heat flux from the ocean to the atmosphere. In the study, sign convention is positive upwards.

2.2.   Methods

2.2.1. Calculation of Niño3.4 Index

In order to describe the evolution of the ENSO cycle, an index is used to define the event. While no single index can adequately explain the diversity of ENSO, the Niño3.4 index is the most widely accepted index for defining the ENSO cycle (Kousky and Higgins 2007). Therefore, this index is chosen as an independent metric through which the variables are compared.

With five different reanalyses, one could use 1) the Niño3.4 index from each model, or 2) a single Niño3.4 index. A single averaged Niño3.4 is chosen so that regressions can be directly compared across different reanalysis data sets. Four of the reanalyses (NCEPR1, NCEPDOE, MERRA, and ERA-Interim) have a prescribed SST while one of the reanalyses (CFSR) uses a coupled system. Each of the reanalyses uses a slightly different SST dataset described in detail in Kumar et al. (2013); however on a seasonal basis the Niño3.4 of each reanalysis differs very little with correlations greater than .98 between the reanalyses for all seasons and for the NDJ season correlations of greater than .997.

The calculation of the Niño3.4 index used is as follows: For each model, the monthly skin temperature is averaged from 5°N -5°S, 170°-120°W. The annual cycle is removed. The Niño3.4 from each of the five reanalyses are then averaged to create a single Niño3.4 index. This is seasonally averaged as a three-month running mean. The three-month averages are then standardized.

2.2.2. Lagged Linear Regressions

ENSO has a distinct seasonal evolution (described in **Section 1.1**). In this study, lagged linear regressions are used to compare each of the variables to the ENSO cycle (defined as Niño3.4). Lagged linear regressions allow us to investigate the temporal evolution of different variables and their impacts on the evolution of ENSO. This differs from the linear regression analysis of surface heat fluxes in reanalyses conducted by Kumar and Hu (2011) in which linear regressions are not seasonally stratified.

In this study, ENSO is chosen to be defined by the season with the most variance, November-December-January (NDJ) (**Figure 3**). This is considered to be the peak of our ENSO events. Because ENSO evolves seasonally lagged regressions can be used to look at the season prior (August-September-October) as the development phase and the season after (February-March-April) as the decay phase. Our index is standardized to show the units "per standard deviation" of the Niño3.4 index. As an El Niño event can be defined as a standard deviation change from normal, the standardized linear regression maps depict the changes occurring during a one standard deviation El Niño. For simplicity, the evolution of ENSO events are discussed in terms of the warm event (El Niño); however, these are linear regressions and to the extent that a linear approximation is appropriate they apply equally but opposite to the cold event (La Niña).

One may ask if linear regressions are an appropriate method for this study. In order to evaluate the linearity of the data compared to Niño3.4 scatterplots were

created at point intervals (not shown). For the three seasons examined in this study, ASO, NDJ and FMA, the shape of the linear approximation appears valid and the El Niño events and La Niña events mirror each other fairly well. During NDJ and FMA, areas west of the dateline are non-linear for net shortwave, precipitation and zonal winds primarily due to strong El Niño events. To determine the extent to which this skews the regressions, the lagged regressions are completed without the two strongest El Niño years (1982/1983 and 1997/1998). The results (not shown) did not significantly influence the regression maps.

3.   Lagged Linear Regression Results

In this chapter, variables that describe the evolution of a typical ENSO event are discussed. This analysis focuses on the seasonal evolution of ENSO; however, ENSO features must be considered with respect to the background seasonal state. For example, a westerly wind deviation could increase latent heat flux out of the ocean if the background mean state is near zero or decrease latent heat flux if the background mean state is strong easterlies. Therefore in addition to describing departures from the annual cycle, the annual cycle is shown to aid in interpretation.

3.1.   First-Order Variables and Precipitation

Here primarily first-order variables that describe the evolution of ENSO are examined. With the exception of precipitation, these variables are constrained by observations with the largest areas of uncertainty occurring in regions of few observations. In all reanalyses in this study precipitation is not constrained by

observations, as precipitation observations are not assimilated into any of the models. An analysis of the surface heat flux variations is reserved for **Section 3.2**.

3.1.1. Sea Surface Temperature (SST)

Figure 4(a-c) shows the seasonal means of SST. Prominent features include the warm pool in the western Pacific, with maximum intensity shifting from north (ASO) to south (NDJ) as peak solar insolation is at its most southern location. Similarly, the cold tongue gradients in the eastern Pacific are strongest in ASO and slowly weaken through FMA.

Figure 4(d-f) shows the seasonal evolution of SST during an ENSO event, as depicted by the seasonal regressions onto the standardized NDJ Niño3.4 index. In the development phase (ASO), the enhanced SST anomalies are confined along the equator in the central and eastern Pacific. The western tropical Pacific is characterized by negative SST anomalies; at ~170°E these anomalies are south of 15°S and extend southeastward to 30°S 150°W. By the ENSO event peak (NDJ), the positive equatorial SST anomalies expand meridionally to around 10°N for most of the northern hemisphere and extend beyond 15°S in the southern hemisphere. As the event decays (FMA), the eastern Pacific SST anomalies ($< 0.6°C$ (std dev)$^{-1}$) decay more rapidly than those in the central Pacific. In the central Pacific, SST anomalies contract towards the equator during boreal spring.

Not surprisingly, the SST anomalies do not differ significantly between the different reanalyses, as SST is highly constrained in the reanalyses, and often include observations from the same inventories. Indeed one of the only minor

differences between the reanalysis SST fields is found near the eastern equatorial

Pacific (near 120°W on the equator) during the decay phase of ENSO, where the

CFSR and ERA-Interim reanalyses suggest a more rapid decay of equatorial SST

anomalies than the other three.

3.1.2. Sea Level Pressure

The seasonal means of sea level pressure (**Fig. 5a-c**) are characterized by a

lower pressure in the western Pacific in the warm pool region and higher pressure

in the eastern Pacific (the climatological Walker circulation). The location of the

lower pressure region corresponds with the seasonal migration of the warm pool.

Also, the equatorial gradient of sea level pressure is at its weakest in FMA, which

corresponds with weakest cold tongue temperature gradients and weakest Niño3.4

variance (**Fig. 3**).

The regressions of sea level pressure **(Fig. 5d-f)** onto the Niño3.4 index depict

the seasonal evolution of sea level pressure during an ENSO event. During ENSO

development (ASO), there is a high-pressure anomaly around the maritime

continent with a lower pressure difference in the central and eastern Pacific which

is most pronounced south of 15°S. As the event peaks (NDJ), the equatorial gradient

reaches its maximum with the high-pressure anomaly intensifying and expanding to

encompass the entire western Pacific; in the eastern Pacific low-pressure anomalies

shift equatorward. As the event decays (FMA), the maximum high-pressure

anomalies shift north of the equator in the western Pacific while the maximum low

pressure anomalies shift poleward in the central Pacific.

The reanalyses exhibit differences with the NCEPDOE having the greatest amplitude variations in mean state and the MERRA and NCEPR1 having the least. Note also the difference in the eastern equatorial Pacific between the 1st and 3rd generation reanalyses, where the higher resolution reanalyses have a better defined equatorial pressure minimum during the peak of an event. In the 1st generation reanalyses, the equatorial pressure minimum is less distinct and blends with off-equatorial features as well.

3.1.3. Precipitation

The seasonal mean states of precipitation are shown in **Figure 6(a-c)**. Consistent with Mitchell and Wallace (1992), the mean state of the Intertropical Convergence Zone (ITCZ) is furthest north in ASO (**Fig. 6a**). In Vincent et al. (2009), the South Pacific Convergence Zone (SPCZ), has been shown to peak in strength and intensity in NDJ which is consistent with **Fig. 6b**. Additionally, all reanalyses show a double ITCZ in the Eastern Pacific in FMA (**Fig. 6c**). The NCEP DOE has the greatest rainfall of the reanalyses, and NCEPR1 has the least. Of the 3rd generation reanalyses, the CFSR has the most rainfall, the MERRA has the least and the ERA-Interim falls in the middle.

Figure 6(d-f) shows the evolution of precipitation anomalies throughout an ENSO event. During the growth stage of an ENSO event (ASO) the ITCZ in the eastern and central Pacific is enhanced and shifts southward in the far eastern Pacific (**Fig. 6d**). This structure is quite different between the 1st and the 3rd generation reanalysis. The 1st generation reanalysis shows increased precipitation in the

central Pacific right on the equator, which contrasts with the increased precipitation on the southern flank of the ITCZ in the other reanalyses (which peaks in intensity at about 7°N). This southward shift is absent from the NCEPR1, and the NCEPDOE places precipitation anomalies on the equator between the dateline and 120°W during the development phase. Here, it is clear that the higher resolution of the 3rd generation reanalyses allows a more precise interpretation of precipitation variations in the eastern Pacific. This is consistent with a study by Bosilovich et al. (2011) which shows that precipitation in 3rd generation reanalyses are better correlated with merged satellite observations, Global Precipitation and Climatology Project (GPCP) and Climate Prediction Center Merged Analysis of Precipitation (CMAP), than previous generation reanalyses.

By the peak of an ENSO event (NDJ), differences between the reanalyses are even more apparent (**Fig. 6e**). The 3rd generation reanalyses show a distinct response of the ITCZ and SPCZ, with positive precipitation anomalies indicating that both convergence zones (CZs) shift closer to the equator and the SPCZ having a more zonal orientation. In contrast, there is little sense of separation between the ITCZ and SPCZ in the NCEPR1 and NCEPDOE reanalyses, and the general impression from those reanalyses is of a single region of positive precipitation anomalies in the central equatorial Pacific (between about 165°E - 110°W). All the reanalyses show negative precipitation anomalies poleward of the CZs and all show an eastward shift of precipitation resulting in a drier far western Pacific and maritime continent.

During FMA, the decay phase of ENSO, all of the reanalyses continue to show an equatorward shift of the convergence zones in the western Pacific. Precipitation anomalies near the dateline have maxima centered south of the equator. In the eastern Pacific, the ITCZ is typically furthest south during FMA (Mitchell and Wallace 1992) and during an ENSO event precipitation extends down to the equator.

In all seasons, the different reanalyses also show very different amplitudes of precipitation anomalies during ENSO, with the NCEPDOE exhibiting the largest amplitude variations and the NCEPR1 showing very weak amplitude variations. Of the 3rd generation reanalyses, the CFSR has the largest amplitude variations, the MERRA has the least and the ERA-Interim falls in the middle (as with the seasonal cycle). Note that many of the differences between the 1st and 3rd generation appear to be related to resolution. With the 1st generation reanalyses having a resolution of ~2° latitude it is difficult to adequately describe the ITCZ which can be less than 2° width in latitude in the eastern Pacific (Bain et al. 2011). In contrast the CFSR and MERRA have 0.5° resolution near the equator which allows a more nuanced interpretation of ITCZ shifts. One should note that the ERA-Interim seems to describe the SPCZ and ITCZ shifts well despite having a resolution of 1.5° near the equator.

3.1.4. Zonal Winds

The zonal winds in the reanalyses have a very similar spatial structure (**Figure 7**). In the seasonal means (**Fig. 7a-c**), there are easterly tradewinds north and south of the equator during all three seasons. The southern lobe is strongest during

ASO and northern lobe is strongest during FMA. In the far eastern equatorial Pacific, there is a region of westerly winds in ASO decreasing through FMA.

Zonal winds show a very similar evolution during ENSO. During the development (ASO) (**Fig. 7d**), the western Pacific shows a region of strong westerly wind anomalies. Depending on the background mean state, these weaken the easterly trades or even shift to westerly winds. As the event progresses (**Fig. 7e-f**), this region of anomalies (centered around 7°N 165°E in ASO) shifts southeast becoming a primarily central south Pacific feature (centered around 5°S 165°W in FMA). In the eastern equatorial Pacific just north of the ITCZ (approximately 8°-15°N east of 130°W), increased easterlies are present during ENSO onset (**Fig. 7d**). As the event peaks (NDJ), this anomaly shifts south and weakens. The extent and intensity of the enhanced easterlies varies among the models.

There are several other features that stand out in the zonal wind regressions. In both hemispheres there is a lobe of westerly anomalies poleward of 15° latitude: in the south Pacific in ASO and in the north Pacific in NDJ strengthening in FMA. In the south Pacific there is an area of enhanced easterlies south of the SPCZ that corresponds with the SPCZ shifting northeast during ENSO. Last there is a region of easterly wind anomalies around the maritime continent during the peak and decay of ENSO.

The reanalyses are very similar with the largest differences occurring near the eastern Pacific ITCZ during the peak and decay phases. The CFSR and NCEPDOE show a larger area of expanded easterlies during NDJ.

3.1.5. Meridional Winds

The meridional wind seasonal mean state (**Fig. 8a-c**) reflects the seasonal march of the ITCZ in the eastern Pacific with a southward movement from ASO into FMA. In the south Pacific, there is a strong northerly wind in the southern hemisphere in ASO, however a southerly component is not seen until NDJ. This is consistent with other research indicating that the SPCZ is stronger in NDJ than ASO (Vincent et al. 2009).

During ENSO, the meridional wind changes correspond to the precipitation changes discussed in **Section 3.1.3** with significant differences between the reanalyses. Overall, during the development phase (**Fig. 8e**), there is a strengthening of the ITCZ convergence and a shift southward; this continues into the peak of the event (**Fig. 8f**). Also, at the peak of the event, the SPCZ displays enhanced convergence and an equatorward shift. By the decay phase, the eastern Pacific is showing little to no enhanced convergence while the SPCZ continues to display enhanced convergence (**Fig. 8f**).

Differences between the reanalyses are significant and are consistent with precipitation differences. The NCEPDOE exhibits the largest amplitude variations and the NCEPR1 shows very weak amplitude variations. Of the 3rd generation reanalyses, the CFSR has the largest variations, the MERRA has the least and the ERA-Interim falls in the middle.
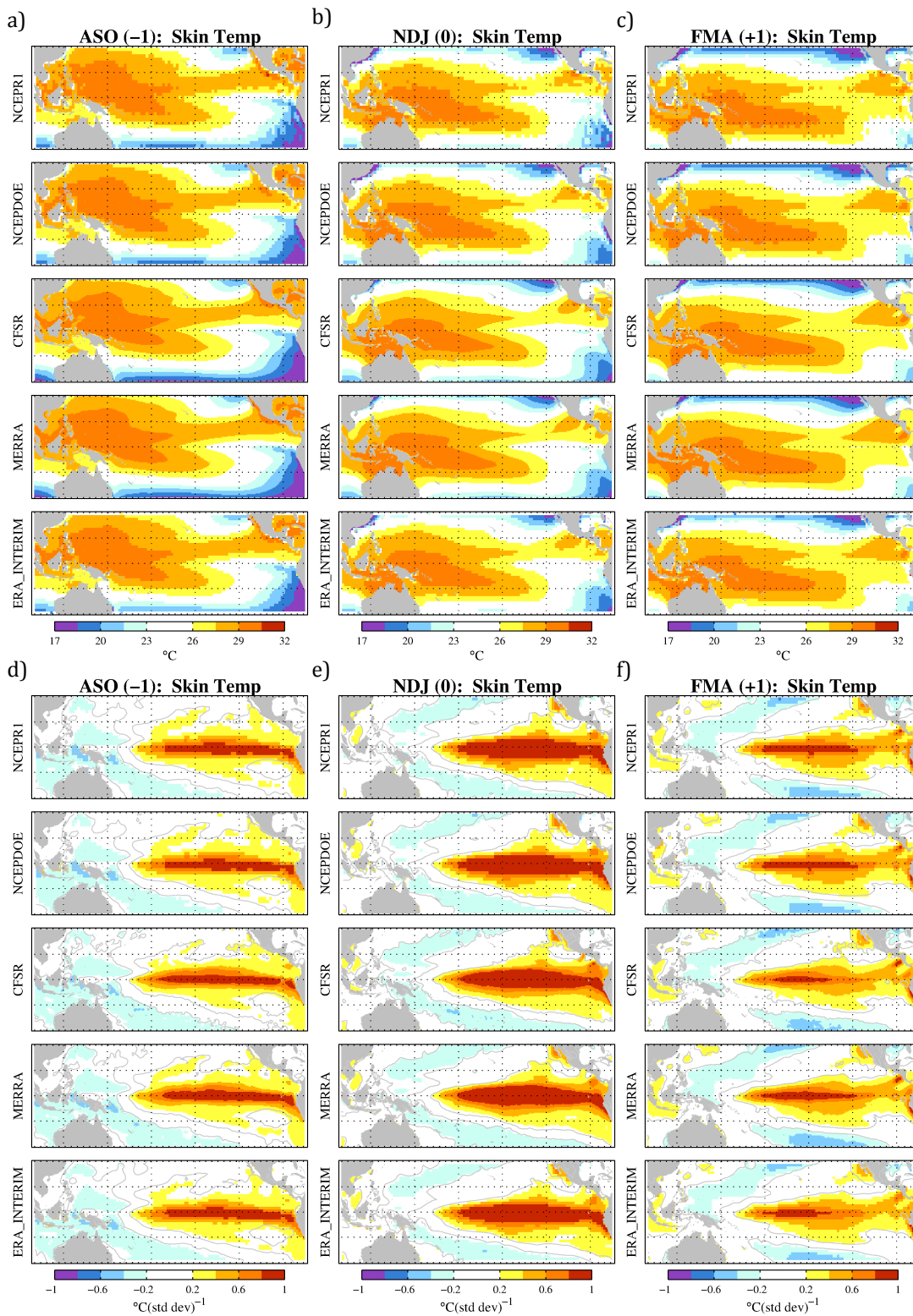
Figure 4: Sea Surface Temperature (SST) - Seasonal Means and Regressions
Seasonal Means for **a)** ASO, **b)** NDJ and **c)** FMA for five reanalyses: NCEPR1, NCEPDOE, CFSR, MERRA and ERA-Interim.   Regressions onto standardized NDJ Nino3.4 for **d)** ASO (lag -1), **e)** NDJ (lag 0) and **f)** FMA (lag +1).
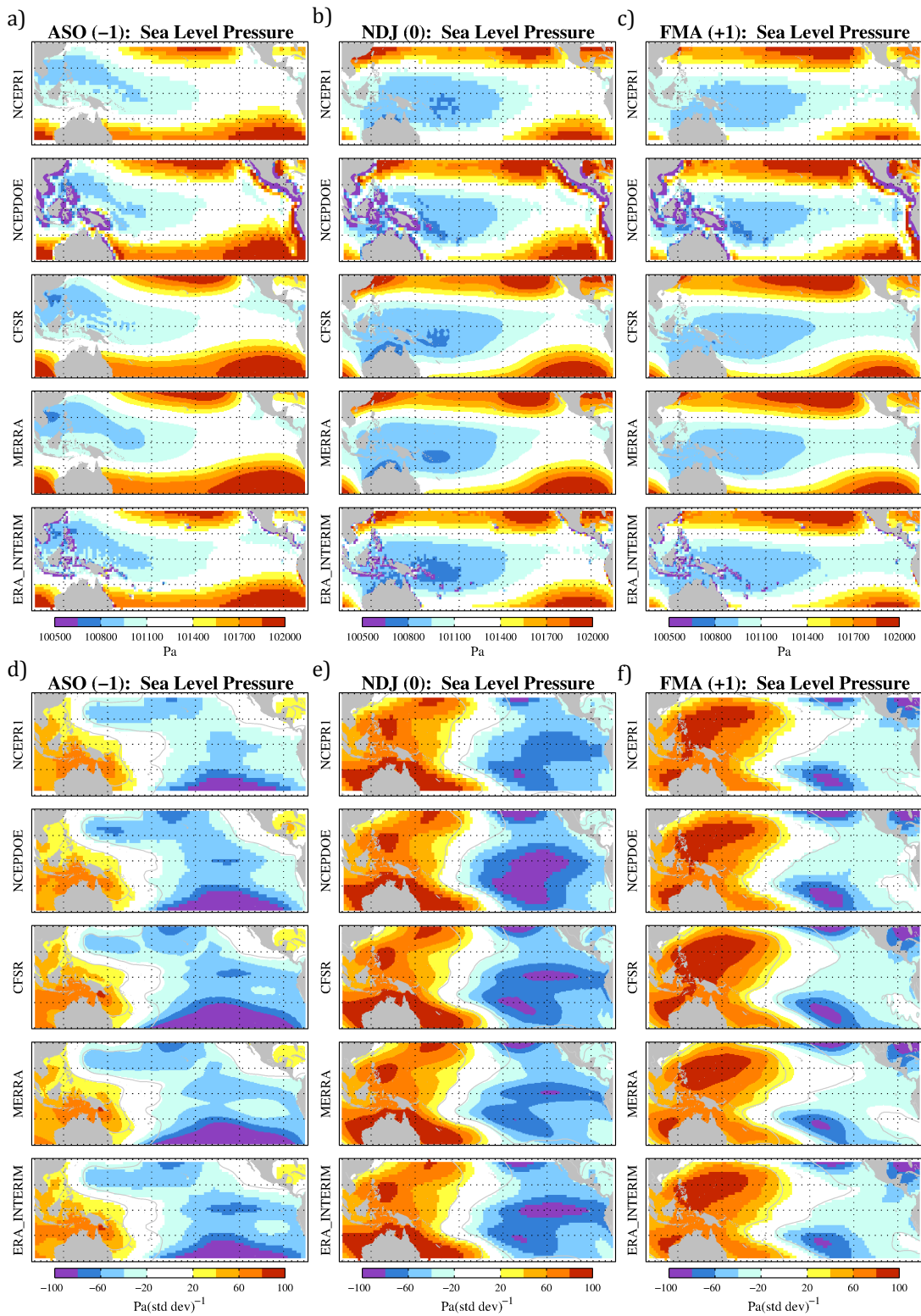
Figure 5: Sea Level Pressure - Seasonal Means and Regressions
Seasonal Means for **a)** ASO, **b)** NDJ and **c)** FMA for five reanalyses: NCEPR1, NCEPDOE, CFSR, MERRA and ERA-Interim. Regressions onto standardized NDJ Nino3.4 for **d)** ASO (lag -1), **e)** NDJ (lag 0) and **f)** FMA (lag +1).
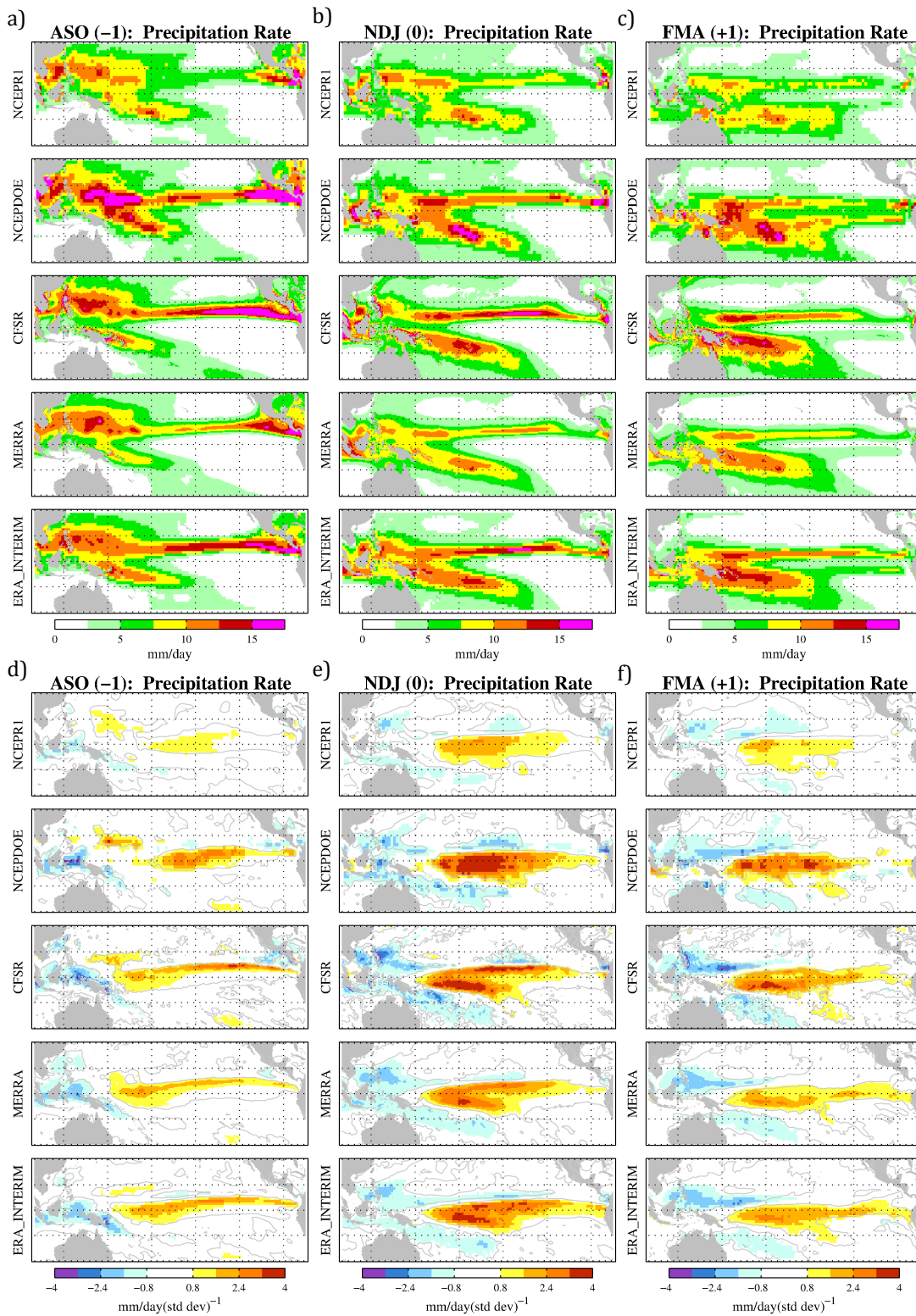
Figure 6: Precipitation - Seasonal means and Regressions
Seasonal Means for **a)** ASO, **b)** NDJ and **c)** FMA for five reanalyses: NCEPR1, NCEPDOE, CFSR, MERRA and ERA-Interim.   Regressions onto standardized NDJ Nino3.4 for **d)** ASO (lag -1), **e)** NDJ (lag 0) and **f)** FMA (lag +1).
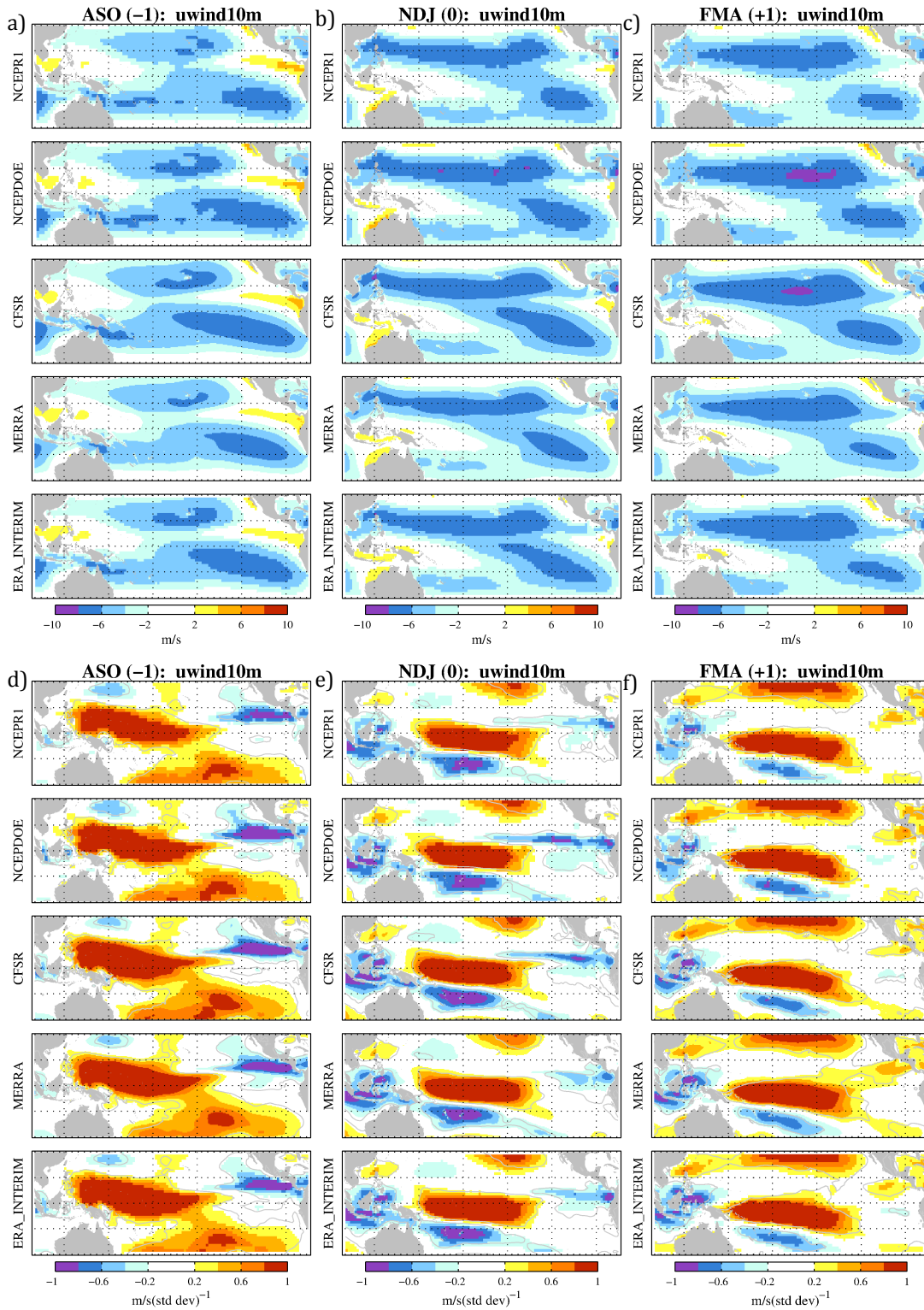
Figure 7: Zonal Winds - Seasonal Means and Regressions
Seasonal Means for **a)** ASO, **b)** NDJ and **c)** FMA for five reanalyses: NCEPR1, NCEPDOE, CFSR, MERRA and ERA-Interim. Regressions onto standardized NDJ Nino3.4 for **d)** ASO (lag -1), **e)** NDJ (lag 0) and **f)** FMA (lag +1).
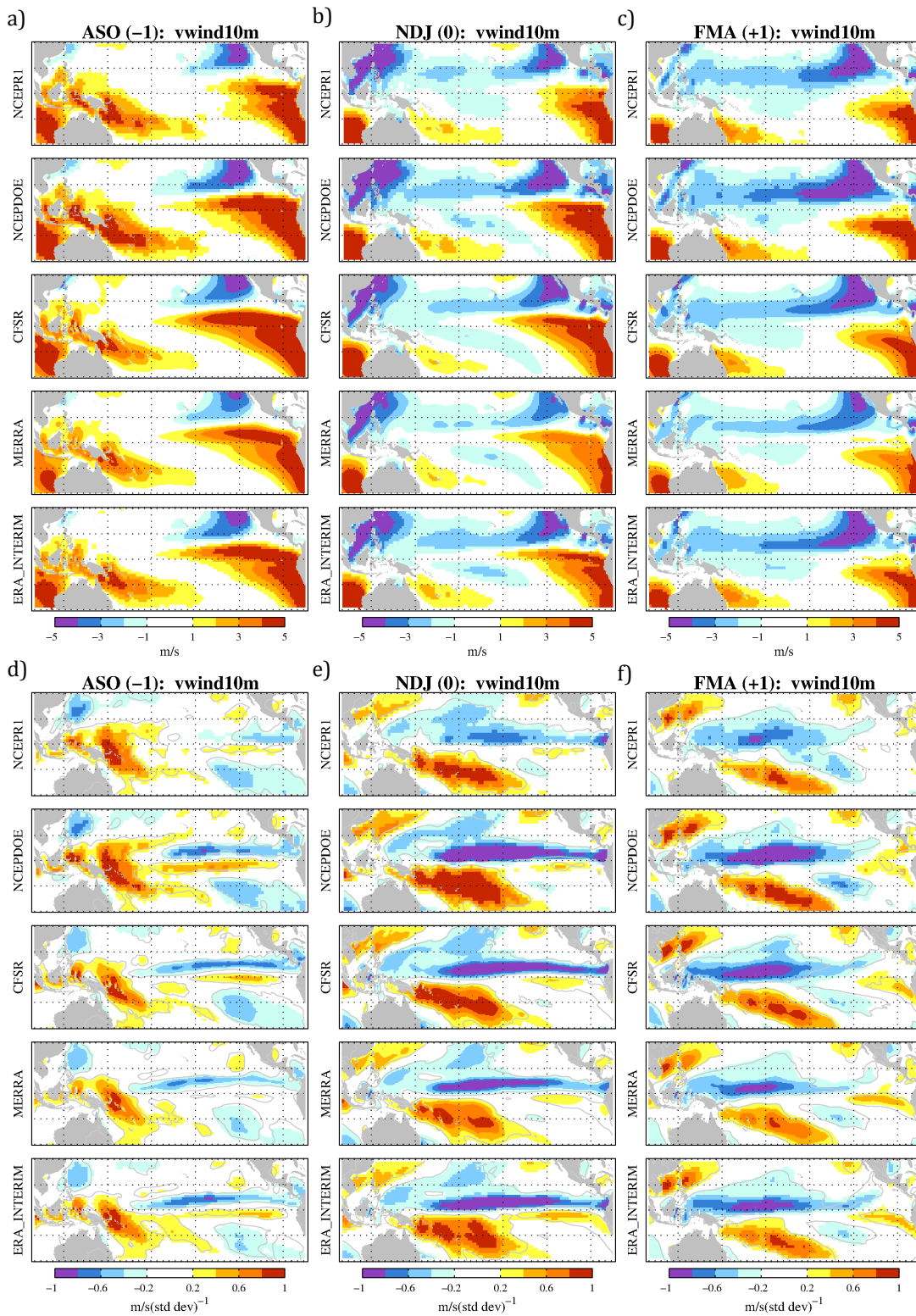
Figure 8: Meridional Winds - Seasonal Means and Regressions
Seasonal Means for **a)** ASO, **b)** NDJ and **c)** FMA for five reanalyses: NCEPR1, NCEPDOE, CFSR, MERRA and ERA-Interim.   Regressions onto standardized NDJ Nino3.4 for **d)** ASO (lag -1), **e)** NDJ (lag 0) and **f)** FMA (lag +1).

3.2.   Thermodynamic (Surface Heat Flux) components

In this section, the surface heat flux components as well as the total heat flux are described. Because surface heat flux components are mostly derived in reanalyses they are much more dependent on the models used in the reanalyses themselves. The different parameterizations, data assimilation methods etc. that are used result in differences among the surface heat flux variations in each reanalysis. In some cases, the differences between seasonal mean states are greater than any differences within ENSO development. In order to best describe this in a reader-friendly manner, the following general format is used in this section: common features in all reanalyses during ENSO, reanalysis differences during ENSO, seasonal mean state differences. Some deviations from this format are made when deemed more reader-friendly.

Sign convention for heat fluxes is as follows and is the same for both mean and anomalous heat fluxes: positive denotes upward heat fluxes (out of the ocean); negative denotes downward heat fluxes (into the ocean).

3.2.1. Latent Heat

Seasonal ENSO Evolution: Common Features in Reanalyses

During the development (ASO) (**Fig. 9d**), positive (upward) latent heat flux anomalies exist along the equator to 10°S from the South American coast to 150°W. South of this region and north (from South American coast to 120°W) are areas of negative (downward) latent heat flux anomalies. West of the dateline two lobes of

negative (downward) heat flux anomalies flank the equator with the extent and intensity varying amongst the reanalyses. These areas of downward anomalous latent heat flux contribute to the warming of SSTs and hence a meridional broadening of ENSO's equatorial SST anomalies. The far western Pacific experiences positive (upward) heat flux anomalies near Indonesia and Australia.

Latent heat flux variations during the peak (NDJ) of an ENSO event are more complex (**Fig. 9e**). There are four significant distinct areas of upward latent heat flux: 1) along the equator as in ASO, 2) north of the equator in the central Pacific (5°-10°N 120°W-165°W), 3) in the north Pacific centered just east of dateline at 15°N, and 4) in the south Pacific center centered just east of dateline at 20°S. Downward latent heat flux anomalies are most pronounced north of 15°N near Philippines and south of the equator between about 0°-15°S, 180°-150°W.

During the decay (FMA), there is pronounced meridional asymmetry (**Fig. 9f**) in the latent heat flux anomalies. North of the equator the latent heat flux is upward, removing heat from the anomalously warm ocean (**Fig. 4f**). Compared to the peak phase, there is little separation between the positive latent heat flux anomalies north of the equator and at the equator between the dateline and 120°W. In the far eastern Pacific (east of about 120°W), upward latent heat flux anomalies primarily occurring in two areas: between 0 and 15°S and north of 15°N. In the south Pacific, anomalous negative latent heat flux continues to allow warming to occur in a line from 5°S 170°W southeast to 15°S 120°W. Further south, an area of positive heat

flux anomalies, which is present at the ENSO peak, expands parallel to the aforementioned region.

Reanalysis Differences in ENSO Evolution

The CFSR and NCEPDOE tend to have the largest amplitude ENSO variations. The MERRA and ERA-Interim show smaller amplitude variations and particularly in the development phase have a smaller spatial extent. NCEP R1 shows lower amplitude variations than the CFSR and NCEPDOE but has similar spatial patterns.

Mean State

The seasonal mean states show similar spatial patterns (**Fig. 9a-c**). The intensities differ with the NCEPDOE consistently showing the largest amplitude variations and the MERRA consistently showing the least. Note that in some areas the differences between reanalyses exceed 40 W/m^2 even amongst 3rd generation reanalyses.

3.2.2. Sensible Heat

Sensible Heat is a minor component of heat budget in the tropical ocean. Seasonal means for most of region are between 0-20 W/m^2 (**Fig. 10a-c**). Differences between reanalyses are minor (<4 W/m^2) (**Fig. 10d-f**). Sensible heat flux variations are shown to provide a full account of the surface heat budget.

3.2.3. Net Shortwave

Net shortwave shows the least consensus among the reanalyses. Incoming shortwave radiation is very model dependent with significant differences among

reanalyses in both the evolution of ENSO and seasonal mean states. This is not surprising given the sensitivity of shortwave radiation variations to differences in cloud distribution, cloud properties, and shortwave radiative transfer schemes, all of which are heavily dependent on model parameterizations.

Seasonal ENSO Evolution: Common Features in Reanalyses

Because of the large differences between shortwave radiation variations among reanalyses, it is more difficult to determine an overall evolution. The following is a description of the more prominent features.

During ENSO development (**Fig. 11d**), there is less incoming shortwave (upward anomalies) along the equator in the central Pacific and western Pacific and more incoming shortwave (downward anomalies) along the equator near Indonesia. At the peak of the event (**Fig. 11e**) these areas intensify and broaden. During ENSO's peak, the central and western Pacific east of 150°E have even less incoming shortwave (upward anomalies) than during the development phase, while the area of downward anomalies around Indonesia expands meridionally and broadens to flank the equator around 150°E. During the decay (**Fig. 11f**), the region of upward anomalies in the equatorial region east of 150°E lessens, while the area of downward anomalies around New Guinea continues to have increased incoming shortwave.

Reanalysis Differences in ENSO Evolution

As stated earlier there are wide variations between the reanalyses during ENSO events (**Fig. 11d-f**). During the entire evolution of an ENSO event the NCEPR1

tends to be zonally confined with less pronounced anomalies. The NCEPDOE

shortwave variations have much larger amplitude. In particular, the area around

Indonesia has larger downward anomalies throughout all three seasons. The

MERRA and the ERA-Interim have the most similar patterns. Of all the reanalyses,

the ERA-Interim has the largest amplitude shortwave radiation anomalies in the

central and western Pacific. It is also the most tightly linked to the precipitation

variations. The MERRA patterns are similar to ERA-Interim but with slightly less

amplitude. Both of these reanalyses have larger downward anomalies in the areas

around Papua New Guinea. During ASO and NDJ, the CFSR shows an area of

downward anomalies around 5°-10°N in eastern and central Pacific not seen in

other reanalyses suggesting a different relationship between clouds, shortwave

radiation and the ITCZ then the other 3rd generation reanalyses. .

Mean State

The seasonal differences between reanalyses are significant with some areas

having a difference of >100 W/m^2 (**Fig. 11a-c**). The 1st generation reanalyses are

similar. Overall, they show much less incoming radiation then 3rd generation

reanalyses. MERRA and ERA-Interim are the most similar with MERRA having more

incoming radiation along the equator around the dateline in all three seasons. The

CFSR is vastly different than other reanalyses. The western Pacific/maritime

continent has large shortwave fluxes into ocean in all seasons. Some regions of the

south Pacific differ by >100 W/m^2. In the eastern Pacific (~east of 110°W), there is

significantly less incoming shortwave not seen in the other 3rd generation reanalyses. This is most pronounced in ASO (**Fig. 11a**).

Overall, differences in mean state need to be considered with regressions. Shortwave regression differences in the reanalyses may be more a factor of different mean states than what is occurring during ENSO evolution.

3.2.4. Net Longwave

Net longwave is a minor component of this budget analysis. However, a few noteworthy items are mentioned.

Seasonal ENSO Evolution:

The variations are less than 4 W/m² with a few exceptions. During ENSO development (**Fig. 12d**), south of Indonesia and north of Australia there is increased outgoing longwave (positive anomalies) in all reanalyses. During ENSO peak (**Fig. 12e**), the central Pacific in the NCEPR1, DOE and CFSR shows an anomalous heat flux into the ocean of 4-8 W/m² that is not seen in the MERRA or ERA-Interim. Pavlakis et al. (2007) indicates this is primarily due to the air temperature and water vapor in the lower atmosphere. Differences in the reanalysis longwave radiation in the tropical oceans are also due to the differences in cloud cover and their vertical structure (Betts et al. 2006). During the decay, the CFSR shows upward anomalies increasing outgoing longwave around the Philippines; this is shown in other reanalyses to lesser extent (**Fig. 12f**). The CFSR also shows downward anomalies at equator on dateline.

Mean state:

Models tend to be between 20-100 W/m^2 outgoing radiation with areas

between 20°N to 20°S ranging from 40-80 W/m^2 (**Fig. 12a-c**). Patterns are similar to

shortwave. The one exception is the NCEPDOE, which has little variation in outgoing

radiation (30-60 W/m^2) over most of the Pacific.

3.2.5. Total Heat Flux

In this section, the surface heat flux defined in **Section 2.2** as

Q$_{surface}$=SWnet+LWnet+SH+LH is examined. As described in the previous sections,

shortwave and latent heat are the dominant terms in ENSO evolution. While the

seasonal evolution of ENSO in the collective reanalyses is discussed, a primary

finding in this project is that vast differences in the shortwave between reanalyses

can give very different interpretations of the surface heat flux's contribution to the

evolution of ENSO.

Seasonal ENSO Evolution:

During ENSO development (**Fig. 13d**), the strong upward equatorial heat flux

anomalies along the equator, in concert with warming the sea surface temperatures,

reflects a dominant role of ocean dynamics in equatorial warming. The westward

extent of upward surface heat flux anomalies is much smaller in the MERRA than the

other reanalyses. This feature is primarily due to the latent heat flux component,

however shortwave also influences western extent. On both sides of the equator

reanalyses show a downward heat flux that broadens the increased equatorial SST

meridionally. This differs considerably amongst reanalyses. The off-equatorial

regions of downward surface heat flux is primarily due to the latent heat component; however, north of equator the CFSR, NCEPDOE, and to a lesser extent ERA-Interim have important contributions from shortwave. Models differ considerably in their representation of surface heat flux variations in the western Pacific and Indonesia during ENSO development. Models tend to show an upward heat flux around 150°E with most showing a net downward heat flux west of this region near Indonesia. This is due to a combination of latent heat and shortwave influences.

As the ENSO event peaks (**Fig. 13e**), the equatorial region is dominated by two regions of upward heat flux anomalies. The first is a large area of upward heat flux along equator east of 150°W extending to 5°-10° S in all reanalyses. This is primarily due to upward latent heat flux anomalies. All reanalyses also show another region of upward heat flux in a diagonal line from around 5°N 180° to 10°N 120°W. Between 180° and 150°E this region is centered more or less on the equator. The amplitudes and positioning of this second feature vary amongst the reanalyses. South of the equator around 10°S-15°S there is a small area of downward heat flux, which continues to broaden SST in Southern Hemisphere.

During the peak of ENSO, the contribution of heat flux components has a distinctly zonal influence with latent heat variations dominating the eastern Pacific, shortwave variations dominating the western Pacific and both latent and shortwave heat fluxes contributing to the central Pacific heat flux. Differences among the reanalyses in total heat flux are largely due to the differences in shortwave heat flux.

As the ENSO event decays (**Fig. 13f**), there is pronounced meridional asymmetry in the surface heat flux. There is an upward heat flux north of the equator between 165°W and 120°W. The amplitude and extent of this heat flux varies among reanalysis. Even as the event decays, downward anomalies along 15°S continue to broaden SSTs southward. The far western Pacific and areas around Indonesia are characterized by downward heat flux anomalies, though as in NDJ (and to some extent ASO), the CFSR has a very different response in this region with upward heat flux anomalies.

Mean state:

In the mean state, there are considerable differences of >75 W/m^2 in some regions (**Fig. 13a-c**). Overall, the MERRA tends to have a stronger heat flux into the ocean in most regions. The CFSR is considerably different in two regions in the south Pacific: the dateline and around 100°W. This is primarily due to mean state differences in shortwave discussed earlier. Around Indonesia, the CFSR tends to have a stronger heat flux into the ocean in all seasons.

Additionally the mean state has seasonal differences. During ASO (**Fig. 13a**), the MERRA shows a strong negative heat flux along the equator across the entire Pacific. The ERA-Interim is similar but with less amplitude. In contrast with the other reanalyses, the NCEPDOE and CFSR show an upward flux in eastern ITCZ and south of the equator. This is primarily due to shortwave differences in these reanalyses. During NDJ (**Fig. 13b**), the differences are primarily in the south Pacific and are dominated by shortwave differences. During FMA (**Fig. 13c**), there are

differences in central Pacific north of the equator. There is a stronger upward heat flux in NCEPR1, NCEPDOE & CFSR due to a combination of reduced incoming shortwave and stronger latent heat due to increased winds as compared to MERRA and ERA-Interim.
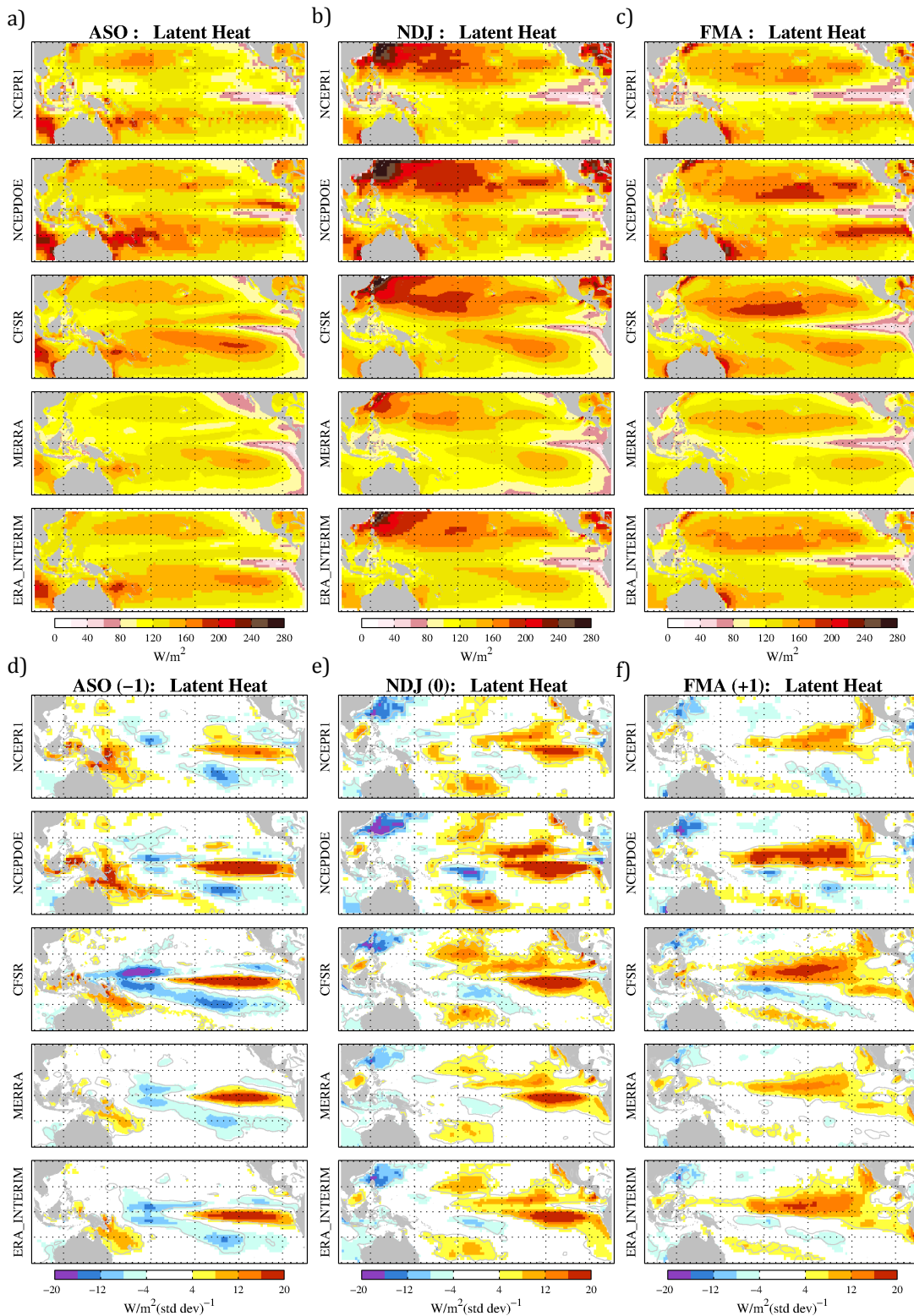
Figure 9: Latent Heat - Seasonal Means and Regressions
Seasonal Means for **a)** ASO, **b)** NDJ and **c)** FMA for five reanalyses: NCEPR1, NCEPDOE, CFSR, MERRA and ERA-Interim. Regressions onto standardized NDJ Nino3.4 for **d)** ASO (lag -1), **e)** NDJ (lag 0) and **f)** FMA (lag +1). Sign convention is positive upwards.
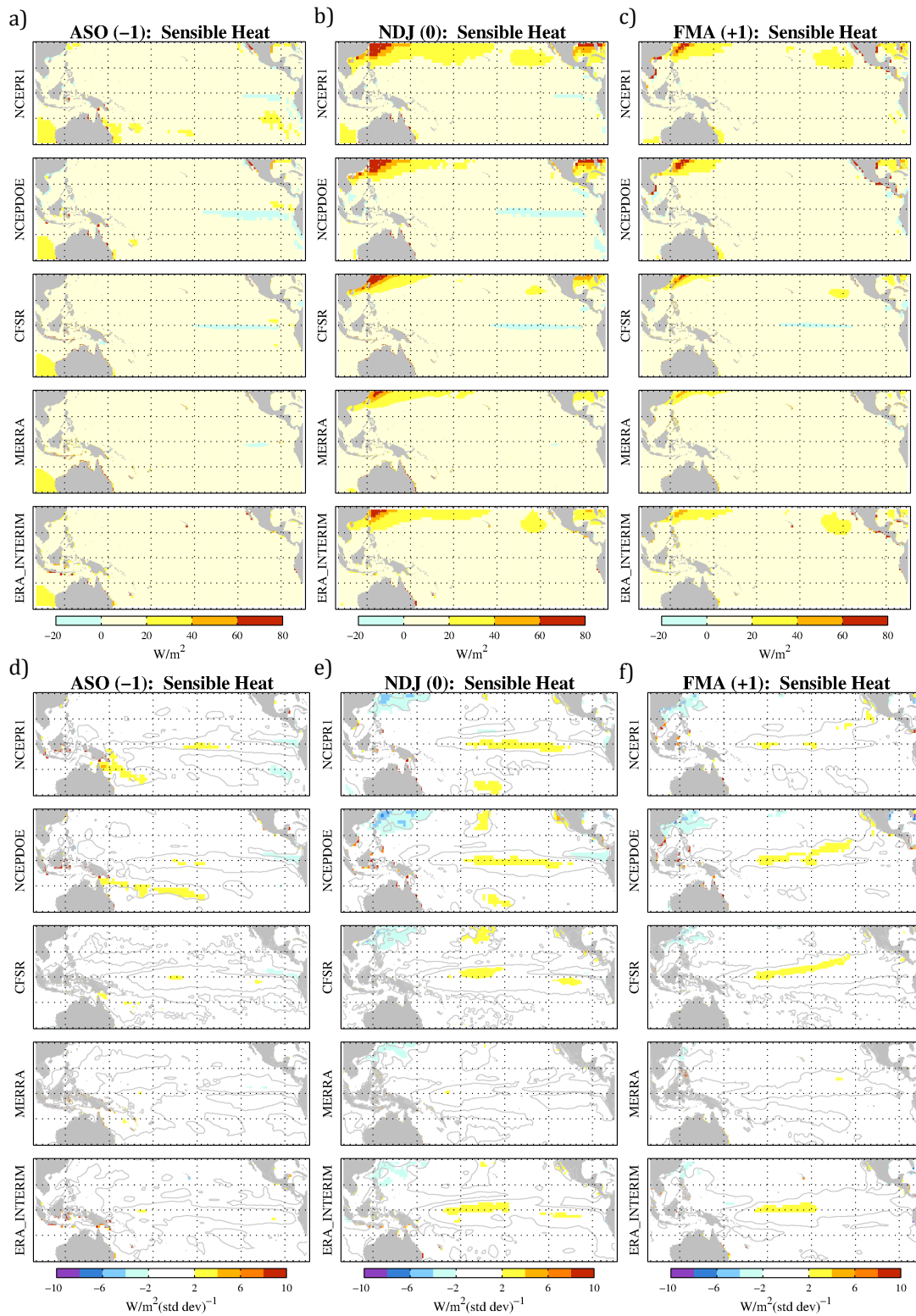
Figure 10: Sensible Heat - Seasonal Means and Regressions
Seasonal Means for **a)** ASO, **b)** NDJ and **c)** FMA for five reanalyses: NCEPR1, NCEPDOE, CFSR, MERRA and ERA-Interim. Regressions onto standardized NDJ Nino3.4 for **d)** ASO (lag -1), **e)** NDJ (lag 0) and **f)** FMA (lag +1). Sign convention is positive upwards.
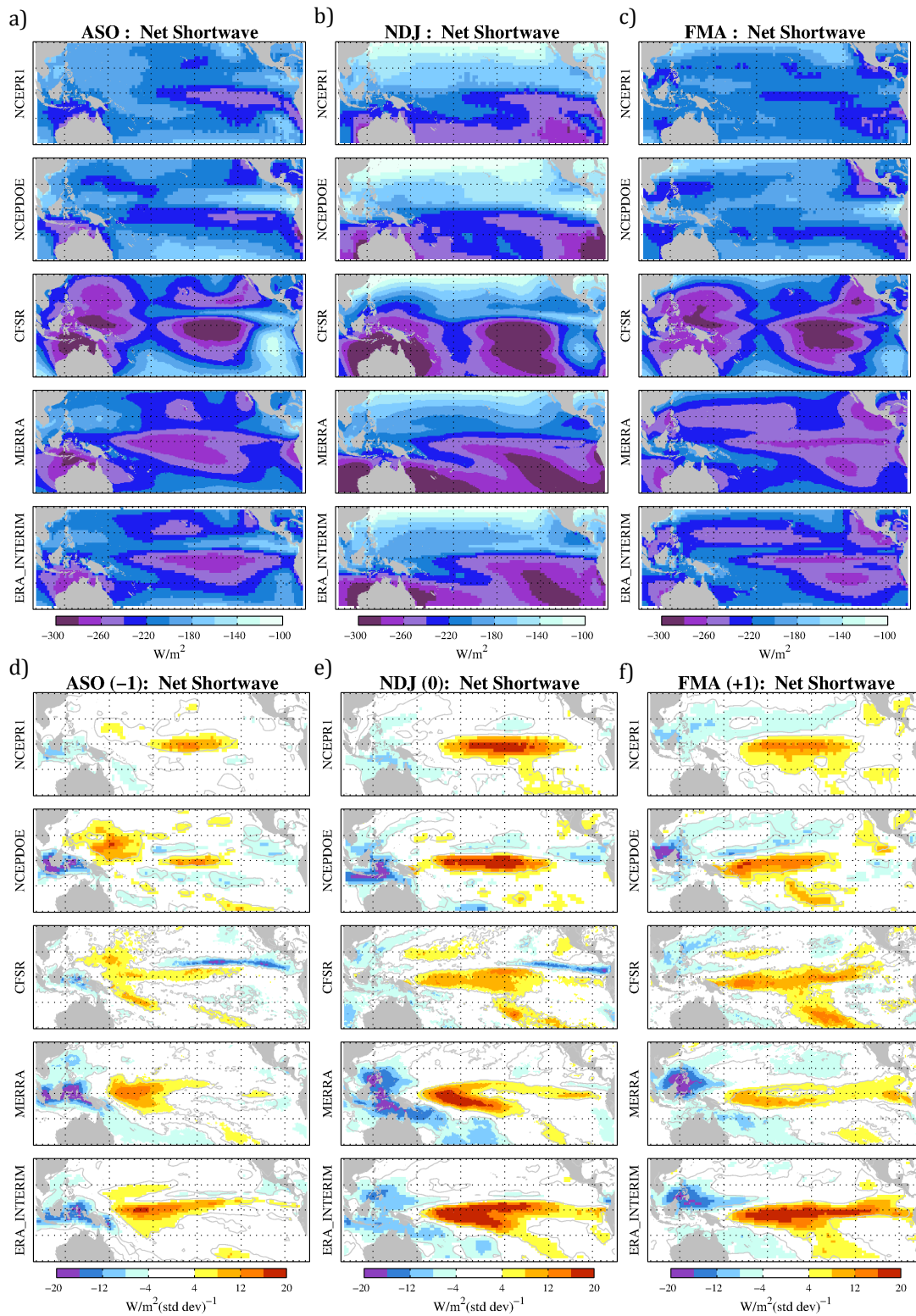
Figure 11: Net Shortwave - Seasonal Means and Regressions
Seasonal Means for **a)** ASO, **b)** NDJ and **c)** FMA for five reanalyses: NCEPR1, NCEPDOE, CFSR, MERRA and ERA-Interim.   Regressions onto standardized NDJ Nino3.4 for **d)** ASO (lag -1), **e)** NDJ (lag 0) and **f)** FMA (lag +1). Sign convention is positive upwards.
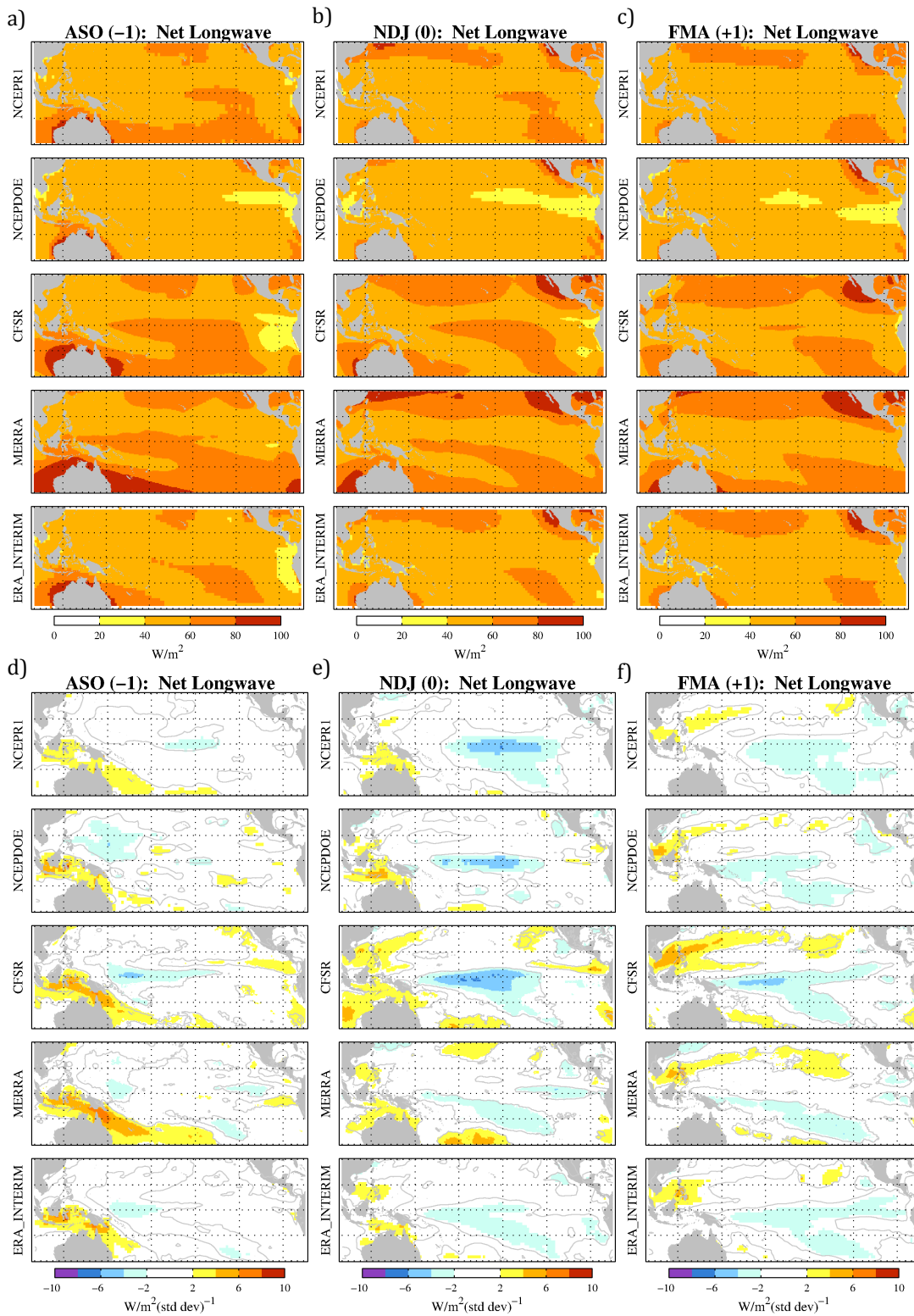
Figure 12: Net Longwave - Seasonal Means and Regressions
Seasonal Means for **a)** ASO, **b)** NDJ and **c)** FMA for five reanalyses: NCEPR1, NCEPDOE, CFSR, MERRA and ERA-Interim. Regressions onto standardized NDJ Nino3.4 for **d)** ASO (lag -1), **e)** NDJ (lag 0) and **f)** FMA (lag +1). Sign convention is positive upwards.
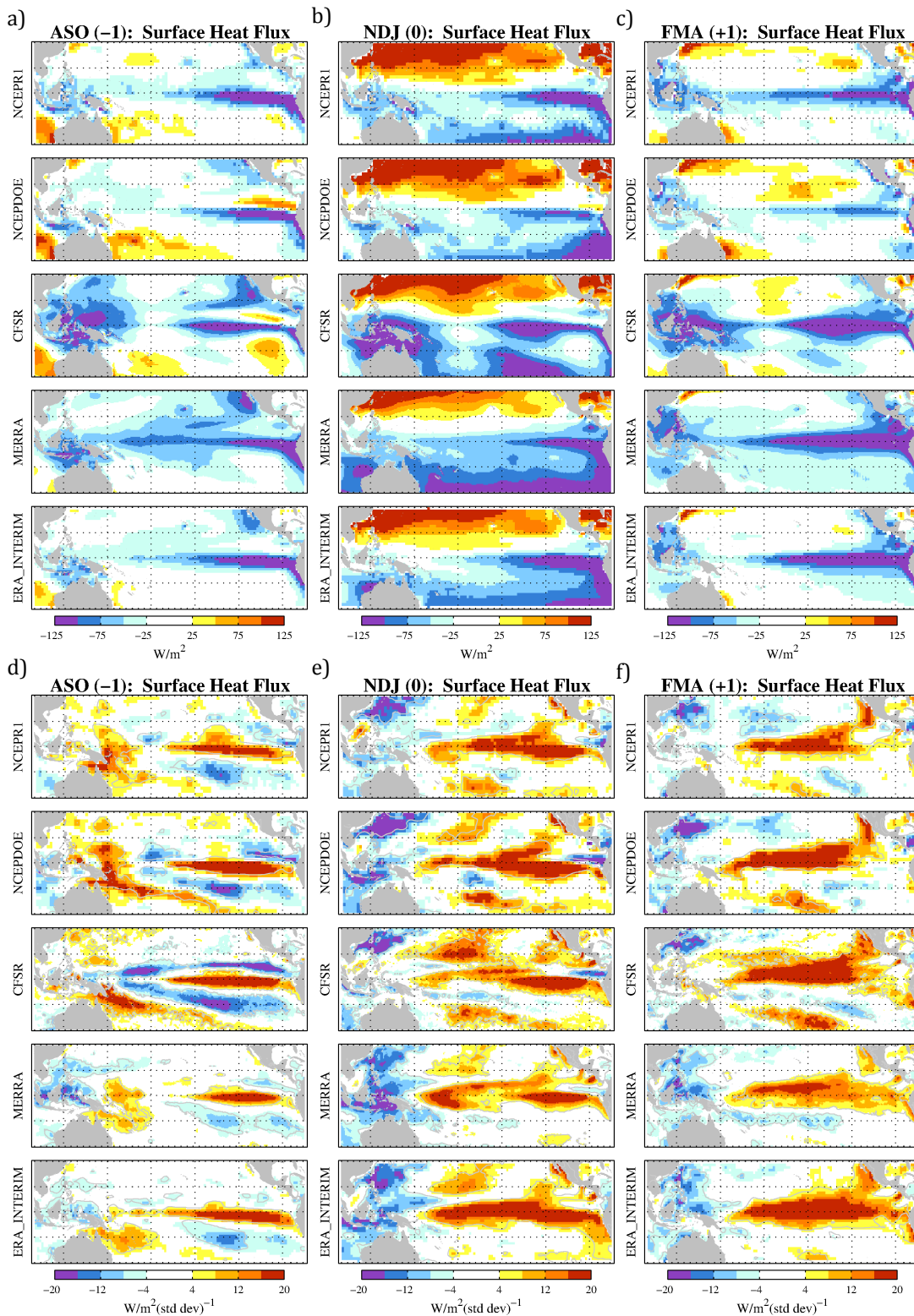
Figure 13: Surface Heat Flux - Seasonal Means and Regressions
Seasonal Means for **a)** ASO, **b)** NDJ and **c)** FMA for five reanalyses: NCEPR1, NCEPDOE, CFSR, MERRA and ERA-Interim.   Regressions onto standardized NDJ Nino3.4 for **d)** ASO (lag -1), **e)** NDJ (lag 0) and **f)** FMA (lag +1). Sign convention is positive upwards.

3.3.   Evaluating Heat Flux Components

The two largest components in the surface heat flux budget are the latent heat flux and net shortwave. The following section attempts to diagnose areas of differences within these components.

3.3.1.   Shortwave vs. Precipitation response during ENSO

The response of shortwave to the Niño3.4 (**Fig. 11d-f**) and precipitation to the Niño3.4 (**Fig. 6d-f**) are similar. A simple explanation for this relationship is that precipitation in this region is mainly thick cloud convective precipitation that reflects shortwave radiation. In areas of increased precipitation during ENSO there is less shortwave radiation reaching the surface; conversely in areas of decreased precipitation there is more shortwave reaching the surface.

In order to further investigate this relationship amongst the reanalyses, a scatterplot of the spatial regressions of shortwave and precipitation is plotted by longitude (**Fig. 14**) and latitude (**Fig. 15**). The scatterplots are for all points located in 15°N–15°S, 100°E–75°W. The scatterplot uses the model's native resolution and as such the 1st generation has the least number of points while the CFSR has the most.

The most striking feature in these plots is the low correlations of the CFSR during ENSO development. It shows a very nonlinear relationship between shortwave and precipitation east of 170°W (**Fig. 14g**) between 3°N and 9°N (**Fig. 15g**); this is the region of the central and eastern Pacific ITCZ. As the ENSO event

progresses into the peak of ENSO (**Fig. 14h)** the most nonlinear relationships are confined further east (generally east of 140°W)**.** By the decay phase the relationship is more linear with little distinction in the relationship between the eastern Pacific and the western Pacific (**Fig. 14&15i**). There is some indication of seasonality differences in the ITCZ in the MERRA (**Fig. 14j-l**) as in the CFSR; however, they are of a much smaller extent. The ERA-Interim is the most linear of all the reanalyses with little difference between the seasons (**Fig. 14&15m-o**).

In the 1st generation reanalyses, the NCEP R1 shows a very linear relationship (**Fig. 14&15a-c**) with the weakest amplitude shortwave and precipitation variations; while the NCEPDOE shows large shortwave and precipitation variations and a less linear relationship (**Fig. 14&15d-f**). A similar analysis is conducted by Kumar and Hu (2011) over all seasons and presumably interpolating all reanalyses to a common resolution. They show similar results; however, in Kumar and Hu (2011) the differences in the CFSR are less apparent. This is attributed to the interpolation of the reanalyses as well as the lack of seasonal stratification.

Several studies (Back and Bretherton 2006; Yuan and Hartmann 2008) show that the convection in the west Pacific warm pool and the east Pacific ITCZ differ in depth. At least one study (Kubar et al. 2007) suggests that the shortwave response to precipitation is different in the western Pacific than the eastern Pacific. While this thesis does not investigate this further, it does provide a possible explanation for the differences in the ITCZ region.
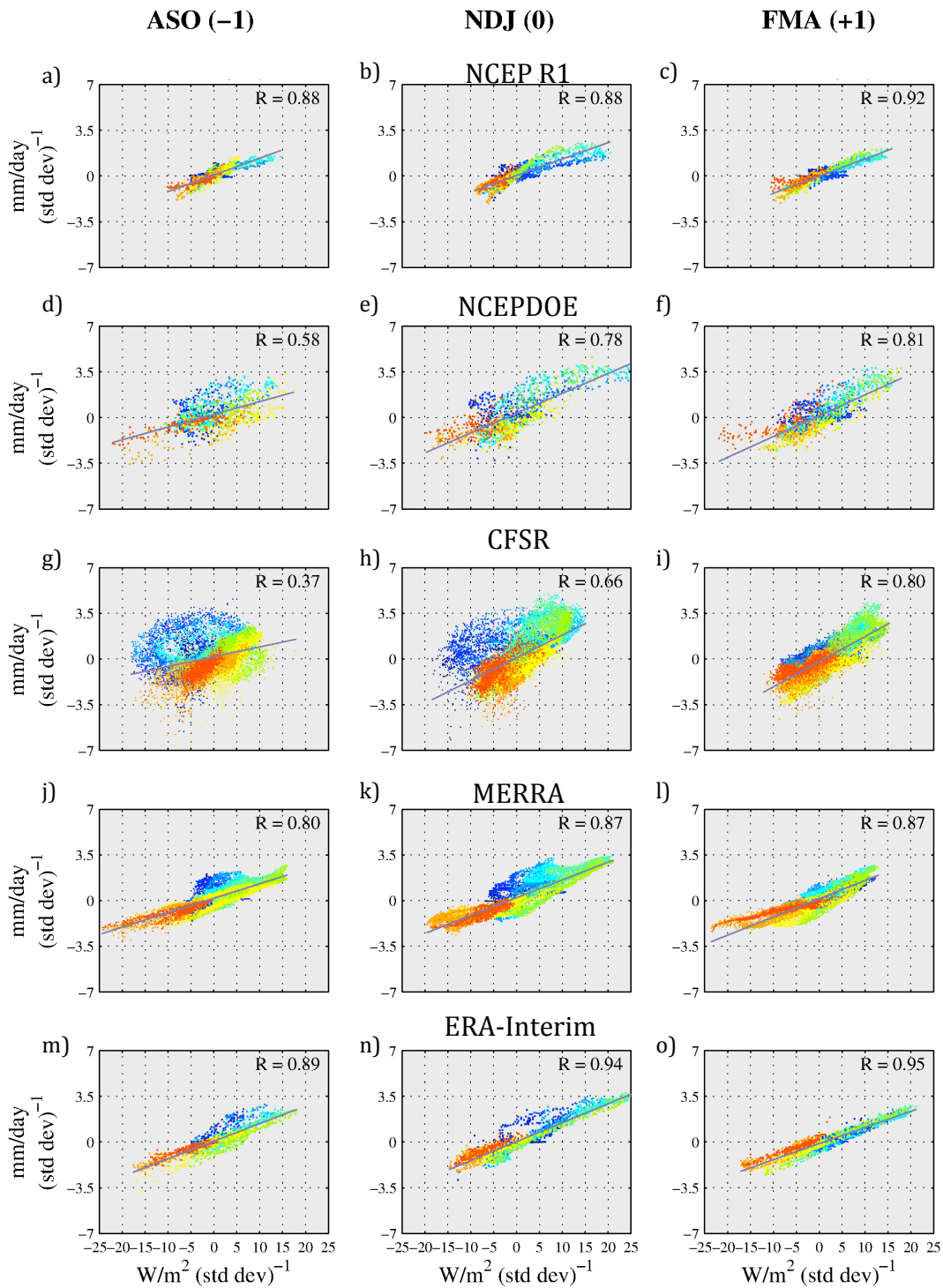
Figure 14: Scatterplots of Shortwave Regressions vs. Precipitation Regressions (Longitude)
Scatter of regressions of shortwave vs. precipitation for 15°S-15°N 100°E to 75°W. All landpoints are removed. Color indicates longitude.
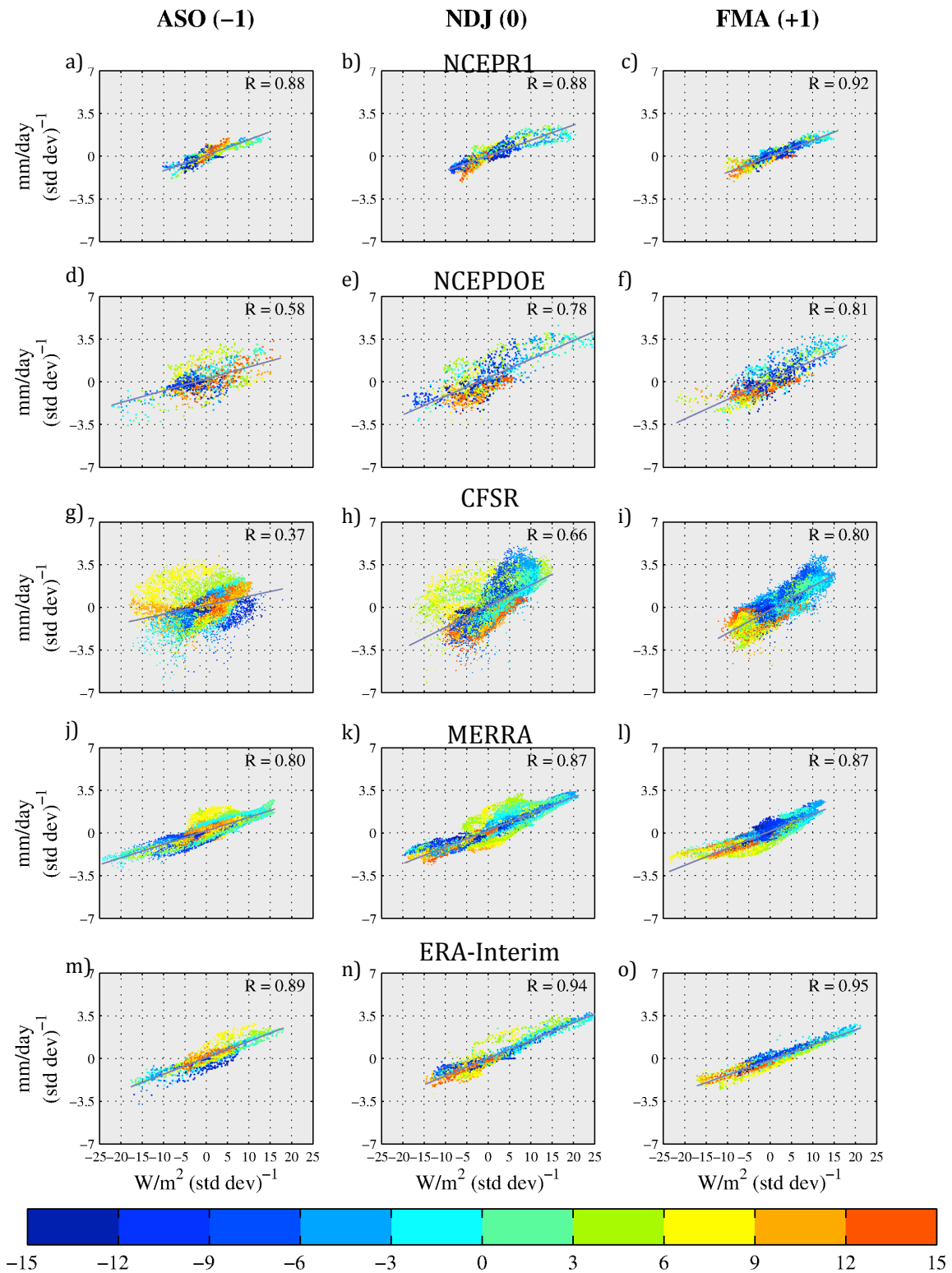
Figure 15: Scatterplots of Shortwave Regressions vs. Precipitation Regressions (Latitude)
Scatter of regressions of shortwave vs. precipitation for 15°S-15°N 100°E to 75°W. All landpoints are removed. Color indicates latitude.

3.3.2. Latent Heat Flux Decomposition

Observational studies show that the latent heat flux damps the anomalously warm temperature anomalies during an ENSO event (e.g. Wang and McPhaden 2000). Our results confirm this, but also show anomalous downward latent heat fluxes to be a contributing factor to ENSO development (**Fig. 9d**) by broadening temperatures meridionally. In this section, the latent heat flux components are examined in an attempt to determine whether near surface humidity or winds are responsible for the variations in the latent heat flux during an ENSO event. This is important as many intermediate models (e.g. Zebiak and Cane 1987; Battisti 1988) represent heat flux as linearly proportionate to temperature and do not include wind dependent changes in their model.

The bulk formula for latent heat flux can be written as:

$$LH = \rho_{air}L_eC_LU(q_{sat} - q_{air}) = KU\Delta q \qquad 2)$$

In this equation, ρ_{air} is the density of air, L_e is the latent heat of evaporation, C_L is the stability-dependent bulk air-sea "drag" coefficient, U is the 10m wind speed, q_{sat} is the saturation specific humidity at the surface SST, q_{air} is the specific humidity calculated at the reference 2m height. For the purposes of this analysis, $\rho_{air}L_eC_L$ is considered to be constant (K). All data are monthly. The 10m wind speed is calculated using

$$U = \sqrt{u^2 + v^2 + (w^*)^2} \qquad 3)$$

where u and v are monthly zonal and meridional wind respectively and w* is a "gustiness factor" which accounts for sub-monthly wind variance. A gustiness factor of 6 m/s is used.

The bulk latent heat flux is linearized in order to examine the individual contributions of 10m winds versus near surface humidity:

$$\delta LH|_{ENSO} = \frac{\partial LH}{\partial \Delta q}|_{CLIM}\delta\Delta q|_{ENSO} + \frac{\partial LH}{\partial u}|_{CLIM}\delta u|_{CLIM} + \frac{\partial LH}{\partial v}|_{CLIM}\delta v|_{CLIM} \cdots \qquad 4)$$

Following the method used in Vimont et al. (2009), the sensitivity of the latent heat flux anomalies to 1) changes in the humidity differences, 2) changes in the zonal wind, and 3) changes in the meridional wind in an El Niño event (represented by standard deviation of the Niño3.4 index) is calculated as follows:

$$\frac{\partial LH}{\partial \Delta q}\bigg|_{CLIM} \delta\Delta q|_{ENSO} = \frac{\overline{LH}}{\overline{\Delta q}} \cdot a_1 \qquad 5)$$

$$\frac{\partial LH}{\partial \Delta u}\bigg|_{CLIM} \delta u|_{ENSO} = \frac{\overline{LH}}{\overline{U}}\bar{u} \cdot a_2 \qquad 6)$$

$$\frac{\partial LH}{\partial \Delta q}\bigg|_{CLIM} \delta v|_{ENSO} = \frac{\overline{LH}}{\overline{U}}\bar{v} \cdot a_3 \qquad 7)$$

where a_1 is the regression of the humidity difference onto the Niño3.4 index, a_2 is the regression of the zonal winds onto the Niño3.4 index, and a_3 is the regression of the meridional winds onto the Niño3.4 index. The latent heat flux variation during ENSO due to linearized components is the total of Eq. (5)+Eq. (6)+Eq. (7).

Figures 16-20 show the **a-c**) Latent Heat regressions (as shown in Figure 7), **d-f**) latent heat flux variations reconstructed from linearized components, **g-i**) latent heat flux changes due to differences in humidity, **j-k**) latent heat flux changes due to zonal wind, and **l-o**) latent heat flux changes due to meridional wind. While there are variations amongst the reanalyses, the focus of this discussion will be on what can be determined by looking at the reanalyses collectively with a few exceptions.

First, the sum of the individual components of the latent heat flux is verified to resemble the actual latent heat flux anomalies by comparing panels (**d-f**) with their corresponding panels (**a-c**) in **Figs. 16-20**. Though differences do exist, three regions are qualitatively reconstructed in the latent heat flux decomposition: (i) anomalous upward latent heat flux along the equator in the central and eastern Pacific, especially during the development and peak phase; (ii) anomalous downward latent heat flux on the equator and around the dateline during development, and extending southeastward during the peak and decay phase; and (iii) anomalous upward latent heat flux in the ITCZ region during the peak and decay phase, around 5°N from the dateline to the eastern edge of the basin. These three areas are the focus herein.

During development phase (ASO), the humidity difference along the equator is responsible for anomalous upward latent heat flux in the eastern and central Pacific as well as weakly contributing to downward latent heat flux in the western Pacific. This anomalous downward latent heat flux in the western Pacific and around the dateline is primarily caused by contributions from the zonal wind. The zonal wind

contribution is responsible for the downward latent heat anomalies in the south Pacific and along the ITCZ in the east Pacific. Although small, all of the reanalyses show a downward latent heat flux near the ITCZ due to meridional winds. The decrease in winds north and south of the equator appear to contribute to meridional expansion of positive SST anomalies away from the equator during NDJ.

During the peak phase (NDJ), differences in humidity continue to intensify upward latent heat fluxes along the equator; however the western extent of this is modified by zonal wind increases resulting in anomalous downward latent heat flux. The winds also contribute to anomalous downward latent heat flux on the equatorward side of the SPCZ, with small contributions from humidity differences as well. North of the equator in the ITCZ region, humidity differences contribute to upward latent heat anomalies in the central and eastern Pacific

One puzzling feature is a gap in increased upward latent heat fluxes centered on 5°N from about 150°W to the eastern edge of the basin shown in all reanalyses (**Fig. 16-20b&e**) during the peak phase. Interestingly, the reanalyses show different reasons for this. The ERA-Interim shows this as a primarily difference in humidity feature (**Fig. 20h**) with some influence from meridional wind reduction (**Fig. 20n**). The CFSR and NCEPDOE show this as primarily a wind feature due to ITCZ movement; zonal winds increasing upward latent heat fluxes north of the ITCZ (**Fig. 17&18k**) and meridional wind inducing downward latent heat fluxes at the ITCZ (**Fig. 17&18n**). In the MERRA, it appears to be primarily differences in humidity (**Fig. 19h**). In the NCEPR1 it is primarily a difference in humidity feature (**Fig. 16h**).

Resolution does not appear to play a large role in the differences, as the CFSR and NCEPDOE are much more closely related then the CFSR and MERRA.

During the decay (FMA), the total latent heat flux decomposition least replicates the latent heat flux regressions particularly in the equatorial central and eastern Pacific. The reanalyses differ, however some generalities can be made. East of 120°W the region of positive (upward) equatorial latent flux anomalies is further south and off of the equator. West of 120°W, differences in humidity create a pronounced meridional asymmetry (**Fig. 16-20i**) with positive latent heat flux anomalies in the northern hemisphere and in the southern hemisphere negative latent heat flux anomalies corresponding with the equatorward shift in the SPCZ. During the decay phase of ENSO, the SPCZ is closest to the equator. This contributes to the meridional asymmetry with a negative (downward) latent heat flux anomalies due to decreased winds (**Fig. 16-20l**). South of the SPCZ there are increased easterlies and positive (upward) latent heat flux anomalies.

There are some concerns, particularly with the winds, in this decomposition. The "gustiness" factor of 6 m/s is chosen to account for all sub-monthly variance. Although not shown gustiness factors of 4 m/s and 2 m/s were also examined; the patterns were similar but showed less of a wind contribution. The gustiness factor is treated as a constant for the entire region, but other studies have shown that it varies significantly particularly in the Convergence Zones (Cronin et al. 2006; Redelsperger et al. 2000). Additionally, in this analysis linearization ignores the covariance of deviations from the mean specific humidity with deviations from the

mean winds ($q'u'$); the extent to which this can be ignored has not been investigated. Last, linearization is based upon small deviations from the mean state. On the western edge of the large wind anomaly in the western Pacific, the mean wind is less than -2 m/s. Therefore using this analysis it is difficult to ascertain how much of the latent heat flux variation is truly due to the wind deviation as the assumptions used are violated. Nevertheless, the linearization of specific humidity does not account for the latent heat flux deviations in this area and the large westerly wind anomaly in a region of westerly winds would decrease the latent heat flux loss from the ocean. Therefore the latent heat flux decomposition is considered to be qualitatively consistent.

NCEPR1 ASO Latent Heat Contributions **NCEPR1 NDJ Latent Heat Contributions** **NCEPR1 FMA Latent Heat Contributions**
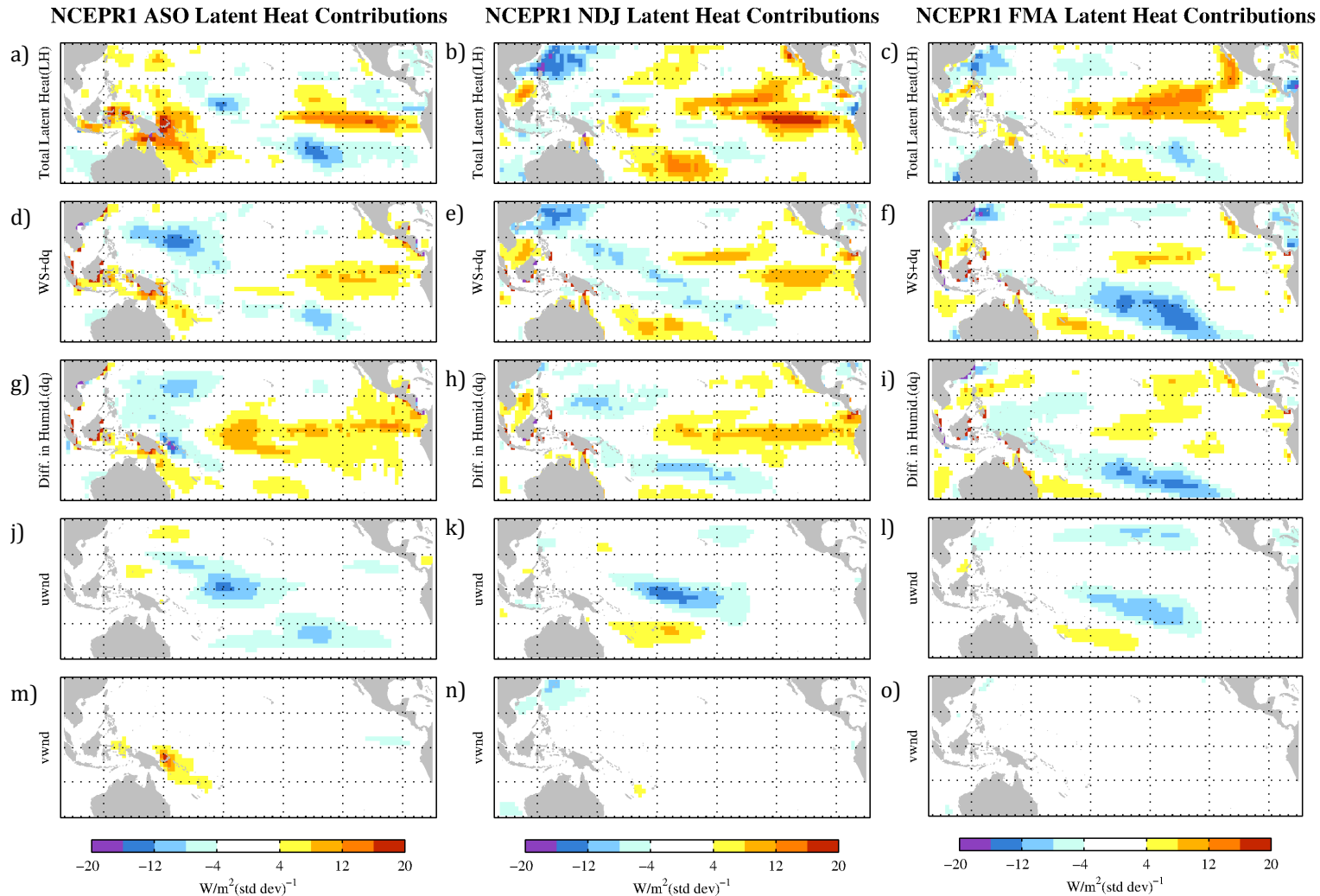
Figure 16: NCEPR1 Latent Heat Decomposition
a-c) Latent Heat regressions (as shown in Figure 7), d-f) latent heat flux variations reconstructed from linearized components, g-i) latent heat flux changes due to differences in humidity, j-k) latent heat flux changes due to zonal wind, and l-o) latent heat flux changes due to meridional wind.

NCEPDOE ASO Latent Heat Contributions

NCEPDOE NDJ Latent Heat Contributions

NCEPDOE FMA Latent Heat Contributions
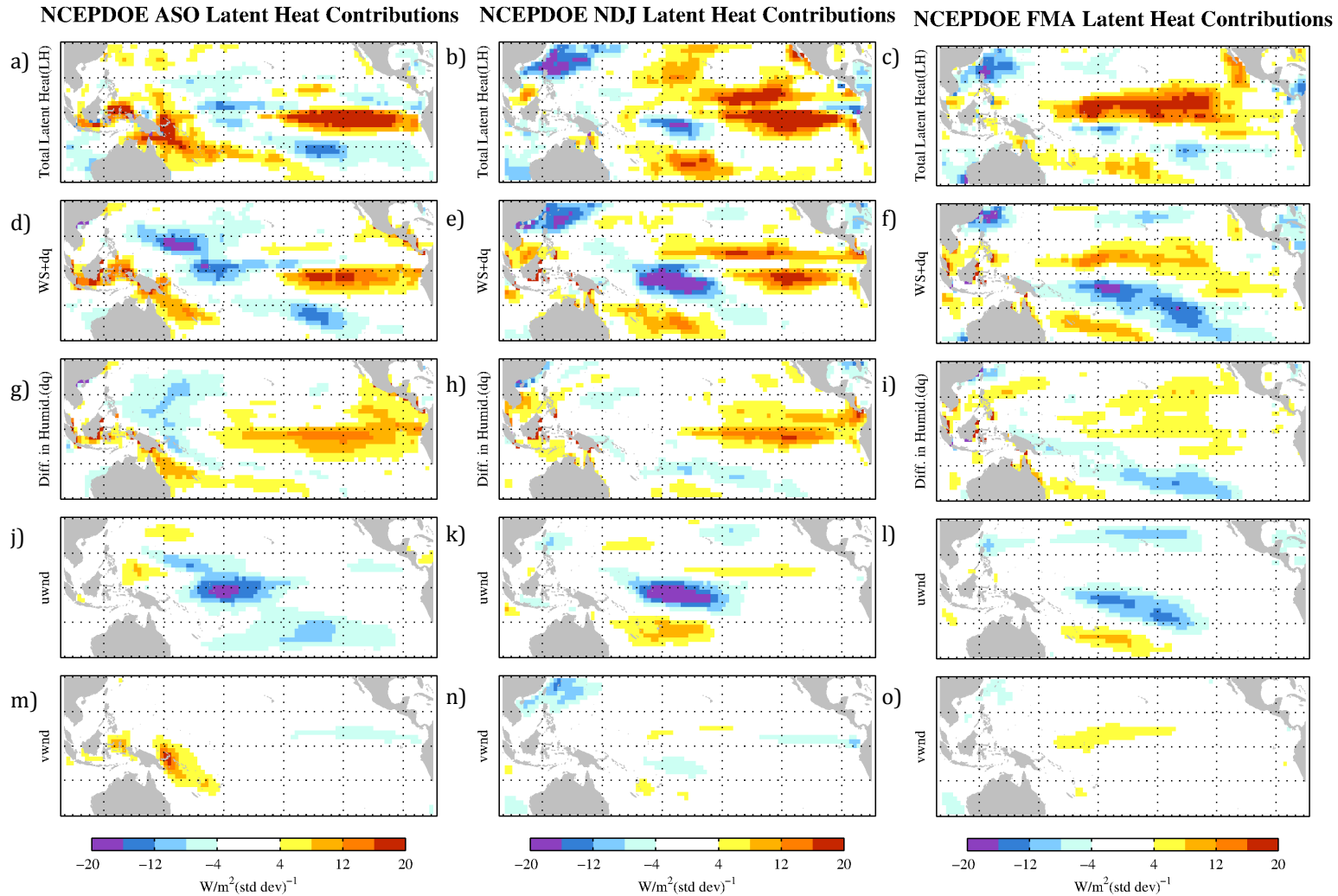
Figure 17: NCEPDOE Latent Heat Flux Decomposition
a-c) Latent Heat regressions (as shown in Figure 7), d-f) latent heat flux variations reconstructed from linearized components, g-i) latent heat flux changes due to differences in humidity, j-k) latent heat flux changes due to zonal wind, and l-o) latent heat flux changes due to meridional wind

CFSR ASO Latent Heat Contributions　　**CFSR NDJ Latent Heat Contributions**　　**CFSR FMA Latent Heat Contributions**
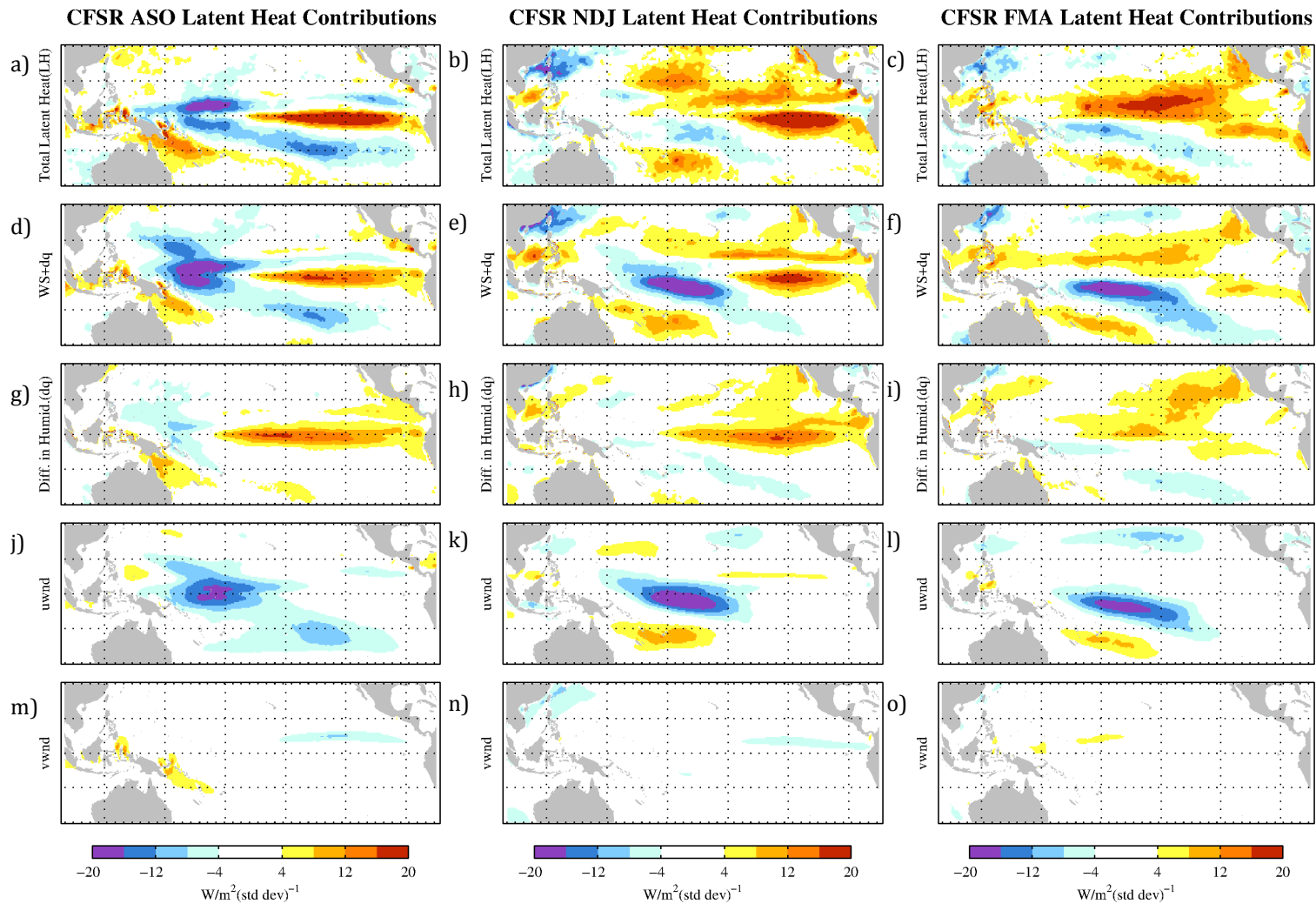
Figure 18: CFSR Latent Heat Flux Decomposition
a-c) Latent Heat regressions (as shown in Figure 7), d-f) latent heat flux variations reconstructed from linearized components, g-i) latent heat flux changes due to differences in humidity, j-k) latent heat flux changes due to zonal wind, and l-o) latent heat flux changes due to meridional wind

MERRA ASO Latent Heat Contributions

MERRA NDJ Latent Heat Contributions

MERRA FMA Latent Heat Contributions
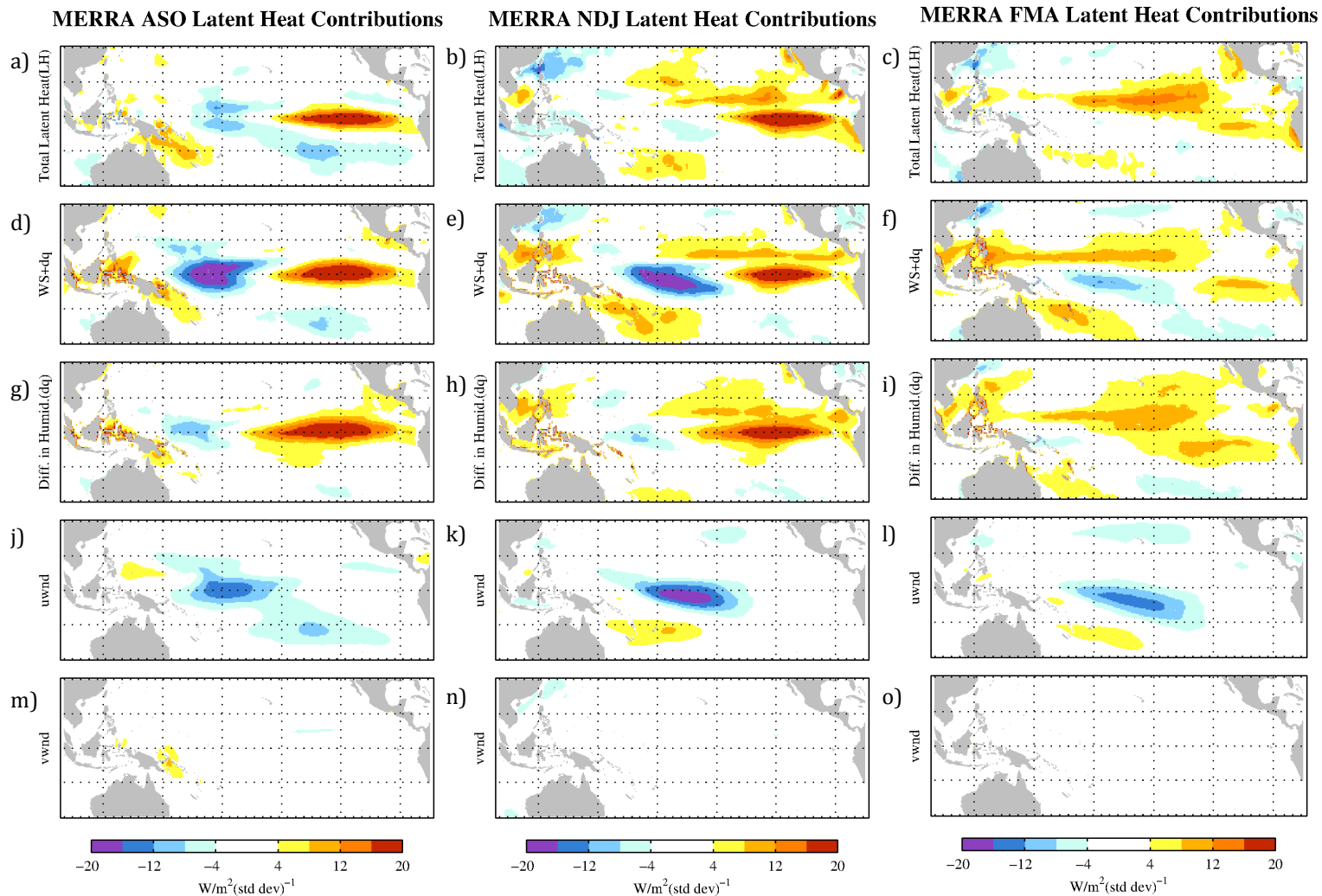
Figure 19: MERRA Latent Heat Flux Decomposition
a-c) Latent Heat regressions (as shown in Figure 7), d-f) latent heat flux variations reconstructed from linearized components, g-i) latent heat flux changes due to differences in humidity, j-k) latent heat flux changes due to zonal wind, and l-o) latent heat flux changes due to meridional wind
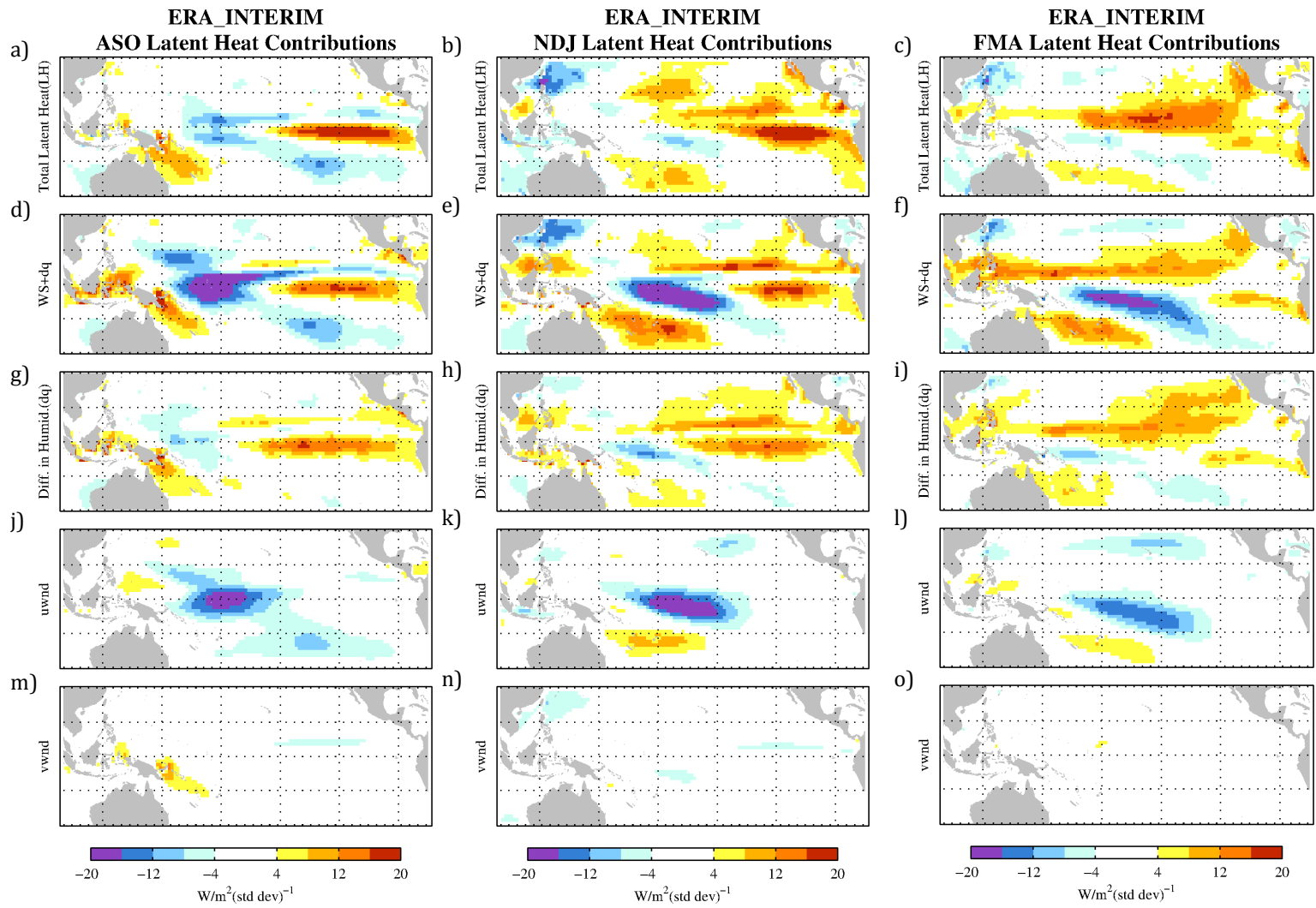
Figure 20: ERA Interim Latent Heat Flux Decomposition
a-c) Latent Heat regressions (as shown in Figure 7), d-f) latent heat flux variations reconstructed from linearized components, g-i) latent heat flux changes due to differences in humidity, j-k) latent heat flux changes due to zonal wind, and l-o) latent heat flux changes due to meridional wind

4.   Conclusions

In this study lagged linear regression analysis is used to explore net surface heat flux variations during ENSO in five reanalysis products: NCEP-NCAR R1, NCEP DOE, ERA-Interim, MERRA and CFSR. The following is a list of our major findings.

First, 3rd generation reanalyses (ERA-Interim, MERRA, and CFSR) provide a much clearer picture of precipitation variations during ENSO (**Fig. 6**). During the development of ENSO, the 3rd generation reanalyses show a southward shift of the ITCZ. During the peak of the event they show a distinct equatorward shift of the ITCZ and SPCZ. This is a vast improvement over the 1st generation reanalyses (NCEPR1 and NCEP DOE), which do not clearly delineate these features.

Second, this analysis supports the view that surface heat flux variations have a role in the meridional warming of SST during ENSO development. In all reanalyses, meridional warming south of the equator is preceded by downward latent heat anomalies (**Fig. 16-20a**) primarily due to decreased easterlies (**Fig. 16-20j**).

In the northeastern Pacific (~0°-10°N) the impact of downward heat fluxes differ among the reanalyses during ENSO development (**Fig. 13d**) with the CFSR having the largest and the ERA-Interim having the least. The contributions of surface heat flux components depend on the model, with the CFSR and NCEPDOE showing a shortwave contribution (**Fig. 11d**) in addition to the zonal winds, meridional winds, and humidity differences shown in all reanalyses (**Fig. 16-20**). Comparisons of shortwave and precipitation further suggest that this is due to different cloud representations within the ITCZ.

This study's conclusion differs from previous studies (Barnett et al. 1991; Wang and McPhaden 2000; Zhang et al. 2007) which indicate that net surface heat flux does not play a role in ENSO development. This may be due to the area of study in the previous analyses. In this study, the area of meridional broadening varies zonally with much of the heat flux into the ocean occurring poleward of the Niño3.4 region. Wang and McPhaden (2000) examine buoy stations along the equator. Zhang et al. (Zhang et al. 2007) focuses on an average of the Niño3.4. Our study does not contradict the assertion that meridional advection is the primary driver within the Niño3.4 as indicated in these studies; it shows that primarily poleward of this region, surface heat flux variations do contribute to the warming.

A rough estimate of the contribution that the net surface heat flux contributes to the warming SSTs during ASO can be made by looking at

$$\Delta T = \frac{Q_{surface}}{\rho_{ocean} C H} \cdot \Delta t \qquad \text{8)}$$

where ΔT is the change in SST, $Q_{surface}$ is the total surface heat flux, ρ_{ocean} is the density of seawater, C is the heat capacity of sea water, H is depth of the mixed layer, Δt is time interval (3 months). Using an estimate of 10 W/m² and a typical mixed layer depth of 80 m for the downward heat fluxes around 15°S 150°W (**Fig. 13d**), SST warming would be approximately .24 K over a three month period. This estimate is equivalent to the warming in this region between ASO (**Fig. 4d**) and NDJ (**Fig. 4e**), and indicates the surface heat fluxes are the primary drivers of warming. This is supported by Zhang et al. (2007) which indicates meridional and zonal

advection in the region is negligible (<.05 K/month). North of the equator near the eastern ITCZ (approximately 5°N east of 150°W), the downward heat fluxes differ considerably among the reanalyses with the CFSR having fluxes >20 W/m², and the ERA-Interim and MERRA having maxima around 8 W/m². This region has a shallower mixed layer. Using an estimate of 40m for the mixed layer and a 10 W/m² downward surface heat flux, the estimated SST warming of .48 K exceeds the approximately .2 K warming occurring. The work by Zhang et al. (2007) indicates that zonal and meridional advection up to .1 K/month; however, this study is not seasonally stratified. The ITCZ and surrounding area is a complicated region; however considering our estimates of surface heat fluxes contributions exceed the observed warming in many areas, the surface heat fluxes should be considered as a factor in warming during ENSO development.

Last, the lagged linear regressions indicate that the southeastward shift of westerly wind anomalies from the western Pacific to south central Pacific may contribute to the decay of an ENSO event, as hypothesized in Harrison and Vecchi (1999). Harrison and Vecchi (1999) found that this meridional movement of the westerly wind anomalies off of the equator allows the eastern Pacific thermocline to shoal and terminate an El Niño event. A recent study by Mcgregor et al. (2012) suggests that this situation is strongly influenced by a well-developed SPCZ in the boreal winter and spring..

In addition to the conclusions on the surface heat flux variations during ENSO, ENSO is used to qualitatively compare the reanalyses. Ideally, this study would be

compared to independent observations. However, the objective of reanalyses is to incorporate all available high-quality observations to produce the best possible product, making it difficult to find an independent dataset with which to compare. As an example, one product that is sometimes used for comparison purposes is OAFlux. OAFlux uses wind, surface temperature, air temperature, and near surface atmospheric humidity from the NCEPR1, NCEPDOE, and ERA40 (a 2nd generation reanalysis) to calculate latent and sensible heat flux. In OAFlux these reanalyses are used "to fill in the data information that satellites are unable to provide and to fill in the gaps that are missed between swaths" (Yu et al. 2008) At least one study, (Brunke et al. 2011), examined reanalyses and other observational datasets by using cruise data not included in reanalysis such as OAFlux and found that the Era-Interim and MERRA outperformed the OAFlux. Adding these uncertainties is beyond the scope of this project.

In order to qualitatively compare the reanalyses this study's results are placed in the context of other studies.

Trenberth et al. (2011b) discusses the close relationship between evaporation and precipitation in the reanalyses and states that most reanalyses overestimate oceanic precipitation. In our analysis, there appears to be internal consistency amongst the reanalyses in terms of zonal winds, latent heat flux and precipitation. Reanalyses with the strongest winds had the greatest latent heat flux and largest precipitation amounts. This is true both in seasonal mean states and ENSO variations. The 3rd generation reanalyses in order from greatest precipitation to

least are: CFSR, ERA-Interim, MERRA. Trenberth et al. (2011b) found the MERRA to the most realistic reanalysis and produced the least precipitation; this is consistent with our findings. Bosolivich et al. (2011) compares the MERRA to merged satellite observations , the Global Precipitation and Climatology Project (CPCP) and Climate Prediction Center Merged Analysis of Precipitation (CMAP), and finds the MERRA and the ERA-Interim are the best performing reanalyses in the tropical Pacific. Again, this is consistent with our findings.

Among the surface heat flux components, shortwave has the largest variance in the reanalyses. The 1st generation reanalyses show far less incoming shortwave than the 3rd generation reanalyses. The MERRA and ERA-Interim showed similar patterns while the CFSR is the outlier with regional differences of >100 W/m^2. Xue et al. (2010) examined the total heat flux and found that the CFSR differs seasonally from other observational products by as much as 100 W/m^2 in the same regions. Wang et al. (2010) shows that the CFSR's lack of clouds over the western warm pool allows too much incoming shortwave radiation in the western Pacific (>50 W/m^2). They also show that the eastern Pacific has too little incoming radiation although they do not elaborate on possible explanations for this. Brunke et al. (2011) compares twelve research cruise to reanalyses (five of which were in our study area); they found that the all-cruise shortwave biases were around 30 W/m^2 for the CFSR, 22 W/m^2 for the ERA-Interim and 6 W/m^2 for the MERRA.

In addition to these significant difference between the seasonal mean states, the shortwave vs. precipitation responses to ENSO (**Fig. 14&15**) suggest that the

CFSR and to some extent the MERRA have a different relationship between these two variables in the ITCZ than in the other regions. This relationship appears to evolve seasonally implying a change in the vertical structure of the clouds during an ENSO event. A thorough investigation into the cloud type and vertical structure would provide more insight on this relationship.

There are some caveats associated with this study. The linear regression is based upon a stationary mean state in the variables. Our analysis of the region shows precipitation in both the MERRA and CFSR increased around 1999. This has been documented in Zhang et al. (2012) and Bosolovich et al. (2011) as a result of the introduction of a new satellite radiances. This is most pronounced in the MERRA. The MERRA also displays a decreasing trend in shortwave into the ocean ~ 10 W/m² over 30 years and longwave showed a slight decreasing trend. Zonal winds and latent heat flux out of the ocean increased during the period in all reanalyses with the increases occurring around 2001. The surface heat flux is stationary in all reanalyses except the NCEPDOE, which shows an increase. To test the role of these discontinuities on our analysis, the data are examined by subtracting the mean from 1979-1998 and 1999-2009 separately and then conducting linear regressions. No significant differences were found.

There have been numerous studies looking at the asymmetry between El Niño and La Niña. While this is a valid concern most of the studies are looking at longer time periods 18-24+ months (e.g. Larkin and Harrison 2002; Okumura and Deser 2010) vs. the nine-month time period looked at in this study. For the nine months

(August-April) analyzed in this study, those studies show that El Niño and La Niña mirror each other for most areas. Still, these differences could be further assessed by performing composite analyses separately on El Niño and La Niña events.

In addition there are concerns with differences between effects with a central Pacific "Modoki" vs. eastern Pacific "canonical" ENSO. The effects of this are assessed in two ways. First, as discussed previously, the scatterplots at individual locations of the variable vs. Niño3.4 are examined to evaluate linearity. During the ENSO peak and decay, there are nonlinearities west of 150°W from 5°S to 10°N in shortwave, zonal winds, and precipitation which indicate the movement in convection in the Western Pacific is different in very strong El Niño events. In addition, the regression analysis is repeated with the two most extreme El Niño events (1982/1983 and 1997/1998) removed. Although some of the values differed, none were large enough to alter the discussion results. Further work could investigate these events individually and look at a non-linear method of evaluating patterns such as cluster analysis.

Last, ocean dynamics were not included in this study. In order to fully assess the extent the surface heat flux contributes to ENSO evolution it should be evaluated in the context of ocean dynamics including an oceanic mixed layer depth. This is another area for future work.

5.   References

Back, L. E., and C. S. Bretherton, 2006: Geographic variability in the export of moist static energy and vertical motion profiles in the tropical Pacific. *Geophys. Res. Lett.*, **33**, L17810, doi:10.1029/2006GL026672.

Bain, C. L., J. De Paz, J. Kramer, G. Magnusdottir, P. Smyth, H. Stern, and C. Wang, 2011: Detecting the ITCZ in Instantaneous Satellite Data using Spatiotemporal Statistical Modeling: ITCZ Climatology in the East Pacific. *J. Clim.*, **24**, 216–230, doi:10.1175/2010JCLI3716.1.

Barnett, T. P., M. Latif, E. Kirk, and E. Roeckner, 1991: On ENSO Physics. *J. Clim.*, **4**, 487–515, doi:10.1175/1520-0442(1991)004<0487:OEP>2.0.CO;2.

Barnston, A., M. Chelliah, and S. Goldenberg, 1997: Documentation of a highly ENSO-related SST region in the equatorial Pacific. *Atmosphere-ocean*, **37**, 367–383.

Battisti, D. S., 1988: Dynamics and Thermodynamics of a Warming Event in a Coupled Tropical Atmosphere-Ocean Model. *J. Atmos. Sci.*, **45**, doi:10.1175/1520-0469(1988)045<2889:DATOAW>2.0.CO;2.

Betts, A. K., M. Zhao, P. A. Dirmeyer, and A. C. M. Beljaars, 2006: Comparison of ERA40 and NCEP/DOE near-surface data sets with other ISLSCP-II data sets. *J. Geophys. Res.*, **111**, D22S04, doi:10.1029/2006JD007174.

Bjerknes, J., 1969: Atmospheric Teleconnections from the Equatorial Pacific. *Mon. Weather Rev.*, **97**, 163–172, doi:10.1175/1520-0493(1969)097<0163:ATFTEP>2.3.CO;2.

Bloom, S. C., L. L. Takacs, A. M. da Silva, and D. Ledvina, 1996: Data Assimilation Using Incremental Analysis Updates. *Mon. Weather Rev.*, **124**, 1256–1271, doi:10.1175/1520-0493(1996)124<1256:DAUIAU>2.0.CO;2.

Bosilovich, M. G., F. R. Robertson, and J. Chen, 2011: Global Energy and Water Budgets in MERRA. *J. Clim.*, **24**, 5721–5739, doi:10.1175/2011JCLI4175.1.

——, J. Kennedy, D. Dee, and A. ONeill, 2012: On the Reprocessing and Reanalysis of Observations for Climate.

Brunke, M. A., Z. Wang, X. Zeng, M. Bosilovich, and C.-L. Shie, 2011: An Assessment of the Uncertainties in Ocean Surface Turbulent Fluxes in 11 Reanalysis, Satellite-Derived, and Combined Global Datasets. *J. Clim.*, **24**, 5469–5493, doi:10.1175/2011JCLI4223.1.

Cronin, M. F., C. W. Fairall, and M. J. McPhaden, 2006: An assessment of buoy-derived and numerical weather prediction surface heat fluxes in the tropical Pacific. *J. Geophys. Res.*, **111**, C06038, doi:10.1029/2005JC003324.

Dee, D., S. Uppala, A. Simmons, and P. Berrisford, 2011a: The ERA-Interim reanalysis: configuration and performance of the data assimilation system. *QJR Meteorol. Soc,*.

Dee, D. P., and S. Uppala, 2009: Variational bias correction of satellite radiance data in the ERA-Interim reanalysis. *Q. J. R. Meteorol. Soc.*, **135**, 1830–1841, doi:10.1002/qj.493.

——, E. Källén, A. J. Simmons, and L. Haimberger, 2011b: Comments on "Reanalyses Suitable for Characterizing Long-Term Trends." *Bull. Am. Meteorol. Soc.*, **92**, 65–70, doi:10.1175/2010BAMS3070.1.

Deser, C., and J. M. Wallace, 1990: Large-Scale Atmospheric Circulation Features of Warm and Cold Episodes in the Tropical Pacific. *J. Clim.*, **3**, doi:10.1175/1520-0442(1990)003<1254:LSACFO>2.0.CO;2.

Harrison, D. E., and N. K. Larkin, 1996: The COADS Sea Level Pressure Signal: A Near-Global El Niño Composite and Time Series View, 1946-1993. *J. Clim.*, **9**, doi:10.1175/1520-0442(1996)009<3025:TCSLPS>2.0.CO;2.

Harrison, D. E., and N. K. Larkin, 1998: El Niño-Southern Oscillation sea surface temperature and wind anomalies, 1946–1993. *Rev. Geophys.*, **36**, 353, doi:10.1029/98RG00715.

——, and G. A. Vecchi, 1999: On the termination of El Niño. *Geophys. Res. Lett.*, **26**, 1593–1596, doi:10.1029/1999GL900316.

Kalnay, E., and Coauthors, 1996: The NCEP/NCAR 40-Year Reanalysis Project. *Bull. Am. Meteorol. Soc.*, **77**, 437–471, doi:10.1175/1520-0477(1996)077<0437:TNYRP>2.0.CO;2.

Kanamitsu, M., W. Ebisuzaki, J. Woollen, S.-K. Yang, J. J. Hnilo, M. Fiorino, and G. L. Potter, 2002: NCEP–DOE AMIP-II Reanalysis (R-2). *Bull. Am. Meteorol. Soc.*, **83**, 1631–1643, doi:10.1175/BAMS-83-11-1631.

Kousky, V. E., and R. W. Higgins, 2007: An Alert Classification System for Monitoring and Assessing the ENSO Cycle. *Weather Forecast.*, **22**, 353–371, doi:10.1175/WAF987.1.

Kubar, T. L., D. L. Hartmann, and R. Wood, 2007: Radiative and Convective Driving of Tropical High Clouds. *J. Clim.*, **20**, 5510–5526, doi:10.1175/2007JCLI1628.1.

Kumar, A., and Z.-Z. Hu, 2011: Uncertainty in the ocean–atmosphere feedbacks associated with ENSO in the reanalysis products. *Clim. Dyn.*, **39**, 575–588, doi:10.1007/s00382-011-1104-3.

——, L. Zhang, and W. Wang, 2013: Sea Surface Temperature–Precipitation Relationship in Different Reanalyses. *Mon. Weather Rev.*, **141**, 1118–1123, doi:10.1175/MWR-D-12-00214.1.

Larkin, N. K., and D. E. Harrison, 2002: ENSO warm (El Nino) and cold (La Nina) event life cycles: Ocean surface anomaly patterns, their symmetries, asymmetries, and implications. *J. Clim.*, **15**, 1118–1140.

Lin, S.-J., 2004: A "Vertically Lagrangian" Finite-Volume Dynamical Core for Global Models. *Mon. Weather Rev.*, **132**, 2293–2307, doi:10.1175/1520-0493(2004)132<2293:AVLFDC>2.0.CO;2.

McGregor, S., A. Timmermann, N. Schneider, M. F. Stuecker, and M. H. England, 2012: The Effect of the South Pacific Convergence Zone on the Termination of El Niño Events and the Meridional Asymmetry of ENSO*. *J. Clim.*, **25**, 5566–5586, doi:10.1175/JCLI-D-11-00332.1.

McPhaden, M. J., 2004: Evolution of the 2002/03 El Niño*. *Bull. Am. Meteorol. Soc.*, **85**, 677–695, doi:10.1175/BAMS-85-5-677.

Mitchell, T. P., and J. M. Wallace, 1992: The Annual Cycle in Equatorial Convection and Sea Surface Temperature. *J. Clim.*, **5**, doi:10.1175/1520-0442(1992)005<1140:TACIEC>2.0.CO;2.

Okumura, Y. M., and C. Deser, 2010: Asymmetry in the Duration of El Nino and La Nina. *J. Clim.*, **23**, 5826–5843.

Pavlakis, K. G., D. Hatzidimitriou, E. Drakakis, C. Matsoukas, A. Fotiadi, N. Hatzianastassiou, and I. Vardavas, 2007: ENSO surface longwave radiation forcing over the tropical Pacific. *Atmos. Chem. Phys.*, **7**, 2013–2026, doi:10.5194/acp-7-2013-2007.

Rasmusson, E. M., and T. H. Carpenter, 1982: Variations in Tropical Sea Surface Temperature and Surface Wind Fields Associated with the Southern Oscillation/El Niño. *Mon. Weather Rev.*, **110**, 354–384.

Redelsperger, J.-L., F. Guichard, and S. Mondon, 2000: A Parameterization of Mesoscale Enhancement of Surface Fluxes for Large-Scale Models. *J. Clim.*, **13**, doi:10.1175/1520-0442(2000)013<0402:APOMEO>2.0.CO;2.

Rienecker, M. M., and Coauthors, 2011: MERRA: NASA's Modern-Era Retrospective Analysis for Research and Applications. *J. Clim.*, **24**, 3624–3648, doi:10.1175/JCLI-D-11-00015.1.

Roberts, J. B., F. R. Robertson, C. A. Clayson, and M. G. Bosilovich, 2012: Characterization of Turbulent Latent and Sensible Heat Flux Exchange between the Atmosphere and Ocean in MERRA. *J. Clim.*, **25**, 821–838, doi:10.1175/JCLI-D-11-00029.1.

Saha, S., and Coauthors, 2010: The NCEP Climate Forecast System Reanalysis. *Bull. Am. Meteorol. Soc.*, **91**, 1015–1057, doi:10.1175/2010BAMS3001.1.

Thorne, P. W., and R. S. Vose, 2010: Reanalyses Suitable for Characterizing Long-Term Trends. *Bull. Am. Meteorol. Soc.*, **91**, 353–361, doi:10.1175/2009BAMS2858.1.

Trenberth, K. E., and Coauthors, 2011a: Atmospheric Reanalyses: A Major Resource for Ocean Product Development and Modeling. *Proc. OceanObs'09: Sustained Ocean Observations and Information for Society Conf., Vol. 2, ESA Publ. WPP-306*, Venice, Italy, 8.

Trenberth, K. E., J. T. Fasullo, and J. Mackaro, 2011b: Atmospheric Moisture Transports from Ocean to Land and Global Energy Flows in Reanalyses. *J. Clim.*, **24**, 4907–4924, doi:10.1175/2011JCLI4171.1.

Vimont, D. J., M. Alexander, and A. Fontaine, 2009: Midlatitude Excitation of Tropical Variability in the Pacific: The Role of Thermodynamic Coupling and Seasonality*. *J. Clim.*, **22**, 518–534.

Vincent, E. M., M. Lengaigne, C. E. Menkes, N. C. Jourdain, P. Marchesiello, and G. Madec, 2009: Interannual variability of the South Pacific Convergence Zone and implications for tropical cyclone genesis. *Clim. Dyn.*, **36**, 1881–1896, doi:10.1007/s00382-009-0716-3.

Wallace, J. M., E. M. Rasmusson, T. P. Mitchell, V. E. Kousky, E. S. Sarachik, and H. von Storch, 1998: On the structure and evolution of ENSO-related climate variability in the tropical Pacific: Lessons from TOGA. *J. Geophys. Res.*, **103**, 14241, doi:10.1029/97JC02905.

Wang, W., and M. J. McPhaden, 2000: The Surface-Layer Heat Balance in the Equatorial Pacific Ocean. Part II: Interannual Variability*. *J. Phys. Oceanogr.*, **30**, doi:10.1175/1520-0485(2001)031<2989:TSLHBI>2.0.CO;2.

Wang, W., P. Xie, S.-H. Yoo, Y. Xue, A. Kumar, and X. Wu, 2010: An assessment of the surface climate in the NCEP climate forecast system reanalysis. *Clim. Dyn.*, **37**, 1601–1620, doi:10.1007/s00382-010-0935-7.

Webster, P. J., and R. Lukas, 1992: TOGA COARE: The Coupled Ocean-Atmosphere Response Experiment. *Bull. Am. Meteorol. Soc.*, **73**, doi:10.1175/1520-0477(1992)073<1377:TCTCOR>2.0.CO;2.

Xue, Y., B. Huang, Z.-Z. Hu, A. Kumar, C. Wen, D. Behringer, and S. Nadiga, 2010: An assessment of oceanic variability in the NCEP climate forecast system reanalysis. *Clim. Dyn.*, **37**, 2511–2539, doi:10.1007/s00382-010-0954-4.

Yu, L., X. Jin, and R. Weller, 2008: *Multidecade Global Flux Datasets from the Objectively Analyzed Air-sea Fluxes (OAFlux) Project: Latent and sensible heat fluxes, ocean evaporation, and related surface meteorological variables*. Woods Hole. Massachusetts, 64 pp.

Yuan, J., and D. L. Hartmann, 2008: Spatial and temporal dependence of clouds and their radiative impacts on the large-scale vertical velocity profile. *J. Geophys. Res.*, **113**, D19201, doi:10.1029/2007JD009722.

Zebiak, S. E., and M. A. Cane, A model El Niño-Southern Oscillation. *Mon. Weather Rev.*, **115**, 2262–2278.

Zhang, L., A. Kumar, and W. Wang, 2012: Influence of changes in observations on precipitation: A case study for the Climate Forecast System Reanalysis (CFSR). *J. Geophys. Res.*, **117**, D08105, doi:10.1029/2011JD017347.

Zhang, Q., A. Kumar, Y. Xue, W. Wang, and F.-F. Jin, 2007: Analysis of the ENSO Cycle in the NCEP Coupled Forecast Model. *J. Clim.*, **20**, 1265–1284, doi:10.1175/JCLI4062.1.

Equatorial Pacific Sea Surface Temperatures | National Centers for Environmental Information (NCEI). https://www.ncdc.noaa.gov/teleconnections/enso/indicators/sst.php (Accessed June 8, 2015).